Faculteit Industriële Ingenieurswetenschappen

master in de industriële wetenschappen: nucleaire technologie

Masterthesis

Experimental Evaluation of the HS-RP200 Optical Fiber Scintillator for Dosimetry in Clinical and Preclinical Radiotherapy

Jorrit Vanmol

Scriptie ingediend tot het behalen van de graad van master in de industriële wetenschappen: nucleaire technologie, afstudeerrichting nucleair en medisch

PROMOTOR :
Prof. dr. Brigitte RENIERS

PROMOTOR :
dr. Gabriel PAIVA FONSECA

COPROMOTOR :
De heer Burak YALVAC

COPROMOTOR :
drs. Roua ABDULRAHIM

Gezamenlijke opleiding UHasselt en KU Leuven

Universiteit Hasselt | Campus Diepenbeek | Faculteit Industriële Ingenieurswetenschappen | Agoralaan Gebouw H - Gebouw B | BE 3590 Diepenbeek

Universiteit Hasselt | Campus Diepenbeek | Agoralaan Gebouw D | BE 3590 Diepenbeek
Universiteit Hasselt | Campus Hasselt | Martelarenlaan 42 | BE 3500 Hasselt

2024
2025

Faculteit Industriële Ingenieurswetenschappen

master in de industriële wetenschappen: nucleaire technologie

Masterthesis

Experimental Evaluation of the HS-RP200 Optical Fiber Scintillator for Dosimetry in Clinical and Preclinical Radiotherapy

Jorrit Vanmol

Scriptie ingediend tot het behalen van de graad van master in de industriële wetenschappen: nucleaire technologie, afstudeerrichting nucleair en medisch

PROMOTOR :
Prof. dr. Brigitte RENIERS

PROMOTOR :
dr. Gabriel PAIVA FONSECA

COPROMOTOR :
De heer Burak YALVAC

COPROMOTOR :
drs. Roua ABDULRAHIM

UHASSELT KU LEUVEN

Preface

This master's thesis marks the culmination of my academic journey and reflects not only my personal efforts but also the invaluable support and guidance I have received along the way.

I would like to sincerely thank my internal promotor, Prof. Dr. Brigitte Reniers, and my external promotor, Dr. Gabriel Paiva Fonseca, for their continuous support, valuable insights, and expert guidance throughout the course of this research. Your direction has been essential to the progress and outcome of this thesis.

My gratitude also goes to my co-promoters, MSc Burak Yalvac and Drs. Roua Abdulrahim, for their constructive feedback, encouragement, and technical expertise, which greatly contributed to the quality and depth of this work.

I am especially grateful to the teams at Maastro and the NuTeC research group at UHasselt for granting me access to their facilities, sharing their knowledge, and offering me the opportunity to conduct tests and experiments crucial to this thesis.

Finally, I wish to thank my family, friends and girlfriend for their unconditional support, patience, and belief in me during this intensive period.

This thesis would not have been possible without the contributions of each of these individuals and institutions. To all of you, thank you.

Jorrit Vanmol

9 June 2025

Contents

List of Tables

List of Figures

Glossary

Abbreviation	Meaning
APD	Avalanche photodiodes
CBCT	Cone-beam Computed Tomography
CTV	Clinical Target Volume
DVH	Dose-volume histogram
EBRT	External Beam Radiotherapy
eBT	Electronic brachytherapy
EPR	Electron Paramagnetic Resonance
ESR	Electron Spin Resonance
FFF	Flattening Filter Free
HDR	High-dose-rate
HS-RP200	HYPERSCINT Research Platform 200
IC	Ionization Chamber
IMRT	Intensity-modulated radiotherapy
kV	kilovoltage
LDR	Low-dose-rate
LET	Linear energy transfer
LINAC	Linear accelerator
LRA	Lateral response artefacts
MLC	Multileaf Collimator
MRI	Magnetic Resonance Imaging
MU	Monitor Unit
MV	megavoltage
OAR	Organs at Risk
OBI	On-board imager
OD	Optical density
OFS	Optical Fiber Scintillators
PDD	Percentage Depth Dose
PDR	Pulsed-dose-rate
PET	Positron emission tomography
PMMA	Polymethyl methacrylate
PMT	Photon multiplier tube
QA	Quality Assurance
RCF	Radiochromic film

RF	Radiofrequency
RGB	Red, blue, green
SBRT	Stereotactic body radiotherapy
SiPM	Silicon photomultipliers
SNR	Signal-to-Noise ratio
SPECT	Single photon emission computed tomography
SRS	Stereotactic radiosurgery
SSD	Source-to-surface distance
TLD	Thermoluminescent dosimeter
TPS	Treatment Planning System
VMAT	Volumetric modulated arc therapy

Abstract in Dutch

Nauwkeurige en real-time dosimetrie blijft een uitdaging binnen de moderne radiotherapie, vooral bij het gebruik van diverse bestralingsmodaliteiten en opstellingen. Dit onderzoek evalueert de HYPERSCINT RP200 (HS-RP200) optische vezel-scintillatordetector (OFS) als flexibel en betrouwbaar dosimetriesysteem voor klinische en preklinische radiotherapie. Het doel was het bepalen van de reproduceerbaarheid, lineariteit en nauwkeurigheid in verschillende toepassingen.

De HS-RP200 werd onder gestandaardiseerde omstandigheden getest in vier modaliteiten: MV LINAC (Varian TrueBeam), HDR-brachytherapie (Bravos afterloader), elektronische brachytherapie (Axxent Xoft) en preklinische X-stralenbestraling (MultiRad 225). Voor de nauwkeurigheidsbepaling werden de OFS-metingen vergeleken met alaninedosimetrie en radiochromische film als referentiemethoden.

Bij de LINAC- en HDR-metingen vertoonde de detector uitstekende reproduceerbaarheid ($< 1\%$) en lineariteit (afwijking $< 1\%$). De nauwkeurigheid kwam goed overeen met alaninedosimetrie, terwijl bij filmdosimetrie afwijkingen door veroudering werden vastgesteld. Voor Xoft bleef de reproduceerbaarheid binnen 1% en toonde de PDD-analyse goede overeenstemming met de theorie. In MultiRad bleef de reproduceerbaarheid binnen 1%, was de lineariteit sterk en stemden de resultaten goed overeen met alanine. Deze bevindingen bevestigen de HS-RP200 als een nauwkeurige en betrouwbare real-time dosimeter voor uiteenlopende radiotherapietoepassingen.

Abstract in English

Accurate and real-time dose measurement remains a key challenge in modern radiotherapy, especially across different irradiation modalities and setups. This study addresses the need for flexible, high-precision dosimetric tools by evaluating the performance of the HYPERSCINT RP200 (HS-RP200) optical fiber scintillator (OFS) for use in clinical and preclinical radiotherapy. The main objective was to assess its reproducibility, linearity, and accuracy across various applications.

The HS-RP200 was tested under standardized conditions in four radiation modalities: MV LINAC (6 MV photon beams, Varian TrueBeam), high dose-rate (HDR) brachytherapy (Bravos afterloader), electronic brachytherapy (Axxent Xoft), and preclinical X-ray cabinet (Precision MultiRad 225). For the accuracy evaluation, the OFS measurements were compared against alanine dosimetry and radiochromic film as independent reference methods.

The detector showed excellent reproducibility ($< 1\%$ standard deviation) and strong linearity (deviation $< 1\%$) for the LINAC and HDR systems. Accuracy matched well with alanine dosimetry, while film measurements showed deviations due to aging. For Xoft, reproducibility stayed within 1%, and PDD analysis demonstrated good agreement with theoretical values. In MultiRad, reproducibility stayed within 1%, great linearity was observed, and accuracy closely matched alanine. These findings confirm the OFS performance across both clinical and preclinical energy ranges.

Chapter 1

Introduction

1.1 Context

Radiotherapy is one of the principal treatment modalities for cancer, alongside surgery, chemotherapy, and immunotherapy. It delivers ionizing radiation to malignant tissues with the objective of eliminating tumor cells while minimizing exposure to surrounding healthy organs and tissues. Technological advances in treatment planning, imaging, and delivery techniques have significantly improved the precision of modern radiotherapy, enabling highly conformal dose distributions. These allow for dose escalation to the tumor while reducing the radiation dose to organs at risk (OAR), thereby enhancing both treatment efficacy and patient safety.

However, as these technological advances have been implemented, not only treatment efficacy and patient safety have improved, but the overall complexity of radiotherapy has also increased. This introduces new challenges in ensuring that the prescribed dose is accurately and consistently delivered to the target. Deviations between the planned and delivered dose may result in underdosage of the tumor, compromising tumor control, or overdosage, increasing the risk of toxicity to surrounding healthy tissues. Therefore, thorough and accurate dosimetric verification is essential to guarantee treatment quality and patient safety.

Quality assurance (QA) protocols are implemented in radiotherapy workflows to verify all aspects of the treatment process, including imaging, treatment planning, beam delivery, and patient positioning. Within these QA procedures, dosimetry plays a crucial role in verifying whether the dose calculated by the treatment planning system (TPS) corresponds to the dose actually delivered to the patient. In addition to routine QA, dosimetric audits are periodically performed by external organizations to independently assess institutional dosimetric accuracy and to identify potential deviations within the treatment systems.

Traditionally, detectors such as ionization chambers (IC) and thermoluminescent dosimeters (TLD) have been used for dosimetry. While both offer high accuracy, they present important limitations in terms of spatial resolution, real-time monitoring capabilities, and operational efficiency [1], [2] . These limitations have driven the development of alternative dosimetry systems that combine high spatial resolution, real-time dose measurement,

and water equivalence, while maintaining the high accuracy of conventional dosimeters.

These constraints have led to the exploration of alternative dosimetric technologies, with optical fiber scintillators (OFS) emerging as promising candidates. OFSs operate on the principle of scintillation, where ionizing radiation interacts with a scintillating material, resulting in the emission of light. This light is then transmitted through an optical fiber to a photodetector, enabling real-time radiation dose monitoring. The inherent advantages of OFSs include their compact size, immunity to electromagnetic interference, and robustness for in vivo dosimetry and applications requiring high spatial resolution [3], [4].

Scintillators can be categorized into two main types: organic scintillators, which are composed of polymer-based materials, and inorganic scintillators, which consist of crystalline structures. Organic scintillators have an excellent resistance to radiation-induced damage compared to ICs. Due to their minimal polarization effects, they are well-suited for dosimetry applications involving high-energy electrons and remain unaffected by variations in temperature or pressure [5]. Furthermore, organic scintillators demonstrate excellent reproducibility, long-term stability, and high spatial resolution. Their linear response to radiation dose, along with dose-rate independence, makes them particularly effective for characterizing photon and electron beams [6]. Conversely, inorganic scintillators generally yield higher scintillation light output than their organic counterparts [7].

At the NuTeC research group at Hasselt University (UHasselt), research is being conducted on novel dosimetric techniques to support radiotherapy and medical imaging. Recently, NuTeC acquired a HYPERSCINT Research Platform 200 (HS-RP200) from Medscint (organic scintillator), an advanced OFS system that allows real-time dosimetry [3]. This acquisition opens new possibilities for improving the accuracy and reliability of dosimetry in both clinical and preclinical applications.

In collaboration with Maastro, a radiotherapy institute specializing in advanced cancer treatments, systematic studies on the reproducibility, linearity and accuracy of OFSs can be conducted. Through Maastro's facilities, experiments can be conducted using various radiation sources, including a megavolt (MV) linear accelerator (LINAC), brachytherapy devices like the Bravos afterloader, and the Precision MultiRad 225 (Preclinical X-Ray Cabinet). Additionally, the Axxent Xoft (electronic brachytherapy device) is available at NuTeC for further research applications. This partnership makes it possible to compare the HS-RP200 performance with established reference detectors, such as alanine pellets and film dosimetry, assessing its clinical applicability. The aim of conducting this research is to contribute to the further development of innovative dosimetric technologies that enhance both patient safety and the precision of radiotherapy treatments. The scintillator may serve as an excellent tool for both external beam radiotherapy and brachytherapy audits, where it helps verify the absorbed dose through detectors.

1.2 Problem Statement

While optical fiber scintillators have been widely studied and demonstrate potential in dosimetry, research on the HS-RP200 model used in this study remains limited. Although previous studies have explored similar detectors, the specific performance and reliability of this unit in clinical and experimental settings require further evaluation. Gaining a deeper understanding of its characteristics will help refine its application and contribute to future research in radiotherapy dosimetry.

One of the key challenges in using OFSs is the reproducibility of measurements. In a clinical setting, a dosimeter must provide reliable and consistent results, regardless of external factors such as temperature fluctuations or variations in radiation intensity. Therefore, a systematic study is needed to assess the stability of measurements obtained with the HYPERSCINT Research Platform 200 under different experimental conditions.

Another critical factor is linearity. An ideal dosimeter should exhibit a linear response over a wide range of radiation doses. This means that the scintillator's light output must be proportional to the absorbed dose, without saturation effects or deviations at higher dose levels. This aspect is particularly important in high-dose applications such as stereotactic radiation therapy [8].

A third crucial property that needs investigation is the accuracy of the OFS compared to conventional reference methods. Alanine dosimetry is used for 1D dosimetry, whereas film dosimetry is used for 2D measurements. Since film detectors are calibrated through cross-calibration with alanine, alanine serves as the primary reference detector. By comparing the results of the HS-RP200 with these methods, it can be determined whether the OFS represents a clinically acceptable alternative or addition to the existing dosimetry methods.

Furthermore, it is essential to evaluate OFS performance across different radiation treatment modalities. This study focuses on measurements in:

- MV linac (used in conventional radiotherapy);
- Brachytherapy (Bravos afterloader - Ir-192, mean energy of 390 keV [9]- and Axxent Xoft – Irradiation energy: 50 kVp [10]) (where radioactive sources are placed close to or inside tumors);
- Precision MultiRad 225 (Preclinical X-ray cabinet – Irradiation energy: 20 kVp – 225 kVp [11]).

Each of these modalities presents unique dosimetric challenges, such as steep dose gradients and varying radiation spectra [12]. By testing the response of the HS-RP200 under these different conditions, better insights are gained into its applicability in radiotherapy.

This research is essential to determine the feasibility of the HS-RP200 as reliable dosimeter and to further substantiate its potential role in clinical practice. The collaboration between NuTeC, UHasselt and Maastro provides a unique opportunity to critically evaluate this technology and contribute to the advancement of dosimetry innovation in radiotherapy.

1.3 Objectives

The primary objective of this research is to evaluate the performance of the HS-RP200 OFS for radiotherapy dosimetry. Specifically, the study aims to assess its reproducibility, linearity and accuracy across different radiation treatment modalities, including MV linac, brachytherapy (Bravos afterloader, Axxent Xoft), and Precision MultiRad 225 (Preclinical X-ray cabinet). In addition, the energy dependence of the OFS will be investigated using the MultiRad 225.

The main objective is to validate the dosimetric performance of the HS-RP200 optical fiber scintillator by systematically evaluating its reproducibility, linearity, accuracy and energy dependence under different radiation conditions, using alanine pellets and film dosimetry as reference standards.

To achieve this objective, it is divided into four sub-objectives.

1. The first sub-objective is the assessment of reproducibility. The target is to investigate the stability of the dose measurements over repeated exposures under identical conditions and to establish the acceptable variation margin beyond which the OFS is considered unreliable.
2. As a second sub-objective the linearity of the OFS will be evaluated. The OFS response will be measured over a wide range of radiation doses, with the aim to assess whether the light output of the scintillator remains proportional to the absorbed dose without saturation effects or deviations. The linearity performance of the OFS across different radiation treatment modalities will be compared.
3. As a third sub-objective the accuracy of the scintillator will be determined. The dose measurements of the OFS will be compared with those obtained using alanine pellets and film dosimetry, so that the deviation between the OFS measurements and the reference standards can be quantified.
4. The final sub-objective is to investigate the energy dependence of the OFS. The detector will be exposed to radiation across a range of energies, using the MultiRad 225 X-ray cabinet. This study will examine whether the OFS response becomes less accurate at certain energy levels.

The success of this study will be evaluated on the following criteria:

- Reproducibility: the consistency of the HS-RP200 response is assessed through repeated measurements under identical conditions, and the corresponding type A uncertainty is estimated.
- Linearity: the response of the HS-RP200 is evaluated over a clinically relevant dose range to verify its proportionality to the delivered dose and to estimate the associated uncertainty.
- Accuracy: the agreement of the HS-RP200 measurements is evaluated by comparing them to alanine and film dosimetry, considering combined uncertainties and potential influencing factors such as energy and irradiation modality.
- Energy dependence: the response of the HS-RP200 is assessed across different tube

potentials to evaluate its performance under varying photon energies, using the MultiRad 225 system.

However, the study is subject to certain limitations:

- The study will not evaluate the long-term durability or degradation of the HS-RP200 over extended use [13].
- While the results will indicate whether the HS-RP200 is clinically viable, regulatory approval and widespread adoption will require further validation beyond the scope of this research.

By achieving these objectives, this study aims to provide a comprehensive validation of the HYPERSCINT Research Platform 200, supporting its potential adoption as a dosimetric tool in radiotherapy applications and dosimetry audits.

Chapter 2

Theoretical Background

This chapter provides an overview of the physical principles underlying the dosimetric techniques applied in this thesis. The fundamental mechanisms of scintillation, electron paramagnetic resonance, and radiochromic film dosimetry are discussed, along with the basic principles of external beam radiotherapy using linear accelerators and internal radiotherapy using brachytherapy sources.

2.1 Scintillation

2.1.1 Scintillation Mechanism

Scintillation refers to the process by which certain materials emit light following the absorption of ionizing radiation. When energetic charged particles or photons interact with a scintillating medium, they transfer energy through ionization and excitation of the medium's atoms or molecules. The resulting excitation energy is subsequently released as optical photons when the excited states return to their ground state. These scintillation photons typically lie within the ultraviolet or visible spectrum [14], [15].

The overall light yield of a scintillator is generally proportional to the energy deposited by the incident radiation, making scintillators highly suitable for radiation detection and dosimetry. However, not all deposited energy is converted into scintillation light. A substantial portion of the energy is dissipated via non-radiative processes such as lattice vibrations or thermal losses. The fraction of deposited energy that is converted into scintillation light is termed the *scintillation efficiency*, which depends on the scintillator material as well as on the type and linear energy transfer (LET) of the ionizing radiation [14].

Scintillators typically exhibit fast response times, often in the nanosecond range for organic scintillators and in the microsecond range for inorganic scintillators, enabling high temporal resolution in radiation detection applications. The emitted scintillation light is commonly detected using photomultiplier tubes (PMTs), avalanche photodiodes (APDs), or silicon photomultipliers (SiPMs) [14].

2.1.2 Organic vs Inorganic Scintillators

An OFS operates by converting ionizing radiation into optical signals that can be transmitted for real-time dosimetric readout. When ionizing radiation interacts with the scintillating material, energy is deposited, leading to excitation of the scintillator molecules. As these excited states return to their ground state, visible or near-visible light is emitted through the scintillation process. This light is subsequently captured and guided by the optical fiber attached to the scintillator, minimizing signal attenuation during transmission. At the distal end of the fiber, the transmitted light is detected and quantified by a photodetector, providing a real-time measurement of the radiation dose. A schematic representation of the working principle of an OFS is shown in Figure 2.1.

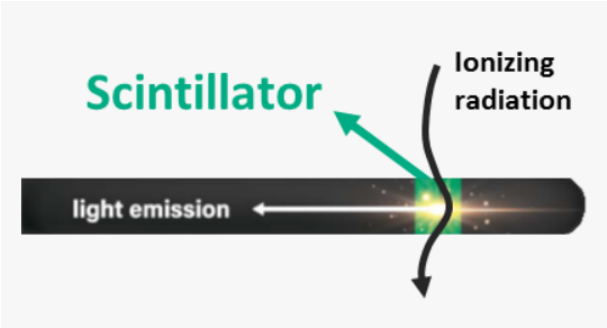

Figure 2.1: Working principle of an OFS [16].

Scintillators are generally categorized into organic and inorganic classes based on their physical composition and scintillation mechanisms.

Organic Scintillators

Organic scintillators are composed of aromatic hydrocarbons, where scintillation arises from de-excitation of π-electron molecular systems. Following energy deposition, molecules are excited to higher electronic states and rapidly undergo internal conversion to the first singlet excited state (S_1). Fluorescence occurs as these excited molecules return to the ground state, emitting scintillation light typically within a few nanoseconds [14].

Key characteristics of organic scintillators include:

- Fast decay times: typically 1 - 10 ns, which provides excellent timing resolution [14].
- Emission spectrum: primarily within 300 - 450 nm, covering the ultraviolet to blue wavelength range [14].
- Low density and low atomic number (Z $\approx$ 5 - 7): resulting in limited detection efficiency for high-energy photons, but high sensitivity for β-particles and charged particles [14].
- Tissue equivalence: due to their similar electron density to water, making them suitable for certain medical applications.
- Physical forms: available as liquids, plastics (e.g., polyvinyltoluene or polystyrene-based), and crystals (e.g., anthracene, stilbene) [14].

The scintillation mechanism in organic scintillators is molecular, and subject to quenching effects at high LET values due to increased ionization density, particularly for heavy charged particles such as protons or alpha particles [14]. Because of their rapid response and flexible manufacturing, organic scintillators are widely used in timing measurements, beta spectroscopy, and fast neutron detection (when hydrogen-loaded) [14].

Inorganic Scintillators

Inorganic scintillators are primarily composed of high-density, high atomic number crystalline materials, such as NaI(Tl), CsI(Tl), BGO, LSO, or $LaBr_3$ [14]. The scintillation process involves the excitation of electrons into the conduction band, followed by de-excitation via activator dopants (e.g., thallium, cerium), which act as luminescence centers embedded in the crystal lattice [14].

Key features of inorganic scintillators include:

- High light yield: often exceeding 50,000 photons/MeV [14].
- Longer decay times: typically ranging from 100 ns to several microseconds [14].
- High density and atomic number ($Z > 30$): providing superior detection efficiency for gamma rays and X-rays [14].
- Superior energy resolution: due to better proportionality between deposited energy and emitted light, leading to excellent spectroscopic performance [14].
- Emission spectra: generally in the range of 400 - 600 nm, depending on the dopant [14].

Due to these properties, inorganic scintillators are widely used in gamma spectroscopy, nuclear medicine imaging (e.g. Positron Emission Tomography (PET), Single Photon Emission Computed Tomography (SPECT)), and high-energy physics experiments [14].

Table 2.1 gives a summary of the differences between organic and inorganic scintillators.

Table 2.1: Summary comparison between organic and inorganic scintillators.

Property	**Organic Scintillators**	**Inorganic Scintillators**
Scintillation mechanism	π-electron molecular de-excitation	Luminescence centers (dopants)
Light yield	Moderate	High
Decay time	$\sim$1–10 ns	100 ns – several μs
Density	Low	High
Atomic number	Low ($Z \approx 5$ - 7)	High ($Z > 30$)
Applications	Timing, beta and charged particles	Gamma spectroscopy, medical imaging
Energy resolution	Poor	Excellent

2.1.3 Comparison with Other Detector Types

In comparison to other radiation detectors, scintillators offer distinct advantages and limitations. Unlike ionization chambers, which provide highly accurate and linear dose

measurements but suffer from slow temporal response and low sensitivity, scintillators exhibit excellent temporal resolution due to their rapid light emission, allowing real-time dose monitoring [14], [15]. Semiconductor detectors, such as silicon or germanium devices, surpass scintillators in energy resolution but typically require complex cooling systems and are more sensitive to radiation damage [14], [15]. Film dosimetry, while offering superior spatial resolution for dose distribution mapping, lacks the real-time readout capability intrinsic to scintillators and requires post-processing [14], [15]. Overall, the combination of high sensitivity, fast response, and reasonable spatial resolution makes scintillators particularly suited for dynamic dose verification and applications where time-resolved measurements are essential [14], [15].

From a dosimetric perspective, scintillators provide near water-equivalent response, minimizing perturbation effects commonly observed with high-Z detectors such as semiconductors [14]. Their minimal energy dependence, particularly in MV photon and electron beams, allows for accurate dose measurements without extensive correction factors [14], [15]. However, careful consideration must be given to potential sources of signal contamination, such as Cerenkov radiation and stem effects in fiber-based scintillation systems [14].

2.2 Alanine Dosimetry

Alanine dosimetry is a well-established method that relies on the formation of stable radiation-induced free radicals in the amino acid L-α-alanine. When exposed to ionizing radiation, alanine crystals undergo chemical changes that result in unpaired electrons. These free radicals can be quantitatively analyzed using Electron Spin Resonance (ESR), also known as Electron Paramagnetic Resonance (EPR) spectroscopy. The intensity of the ESR signal is directly proportional to the absorbed dose, making this technique highly suitable for precise dosimetric applications in radiotherapy [17].

Physical Principle

The underlying physical principle is based on the Zeeman effect. In the presence of a magnetic field, the magnetic moments of the unpaired electrons split into two distinct energy levels, as shown in Figure 2.2. If the system is exposed to a radiofrequency (RF) electromagnetic wave of the appropriate frequency, transitions between these spin states can occur. The resonance condition is described by the equation:

$$E = g\mu_B B = h\nu, \tag{2.1}$$

where g is the proportionality factor, μ_B is the Bohr magneton, B is the magnetic field strength, h is Planck's constant, and ν is the frequency of the applied RF wave [17].

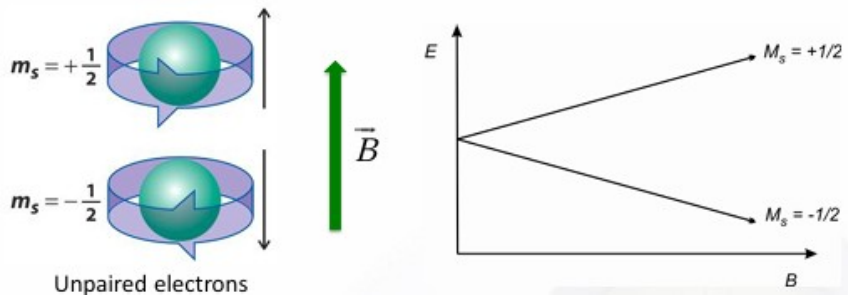

Figure 2.2: Zeeman effect [17].

Since the resonance signal is typically weak, it is enhanced using phase-sensitive detection. This method measures the first derivative of the absorption curve, which improves the signal-to-noise ratio (SNR) and allows for more reliable dose determination at low radical concentrations [17].

Dosimetric Properties

Alanine dosimetry offers several favorable characteristics:

- Nearly tissue-equivalent, with an effective atomic number $Z_{\text{eff}} \approx 6.6$ (compared to 7.5 for water).
- Energy independence in the MV range.
- Dose-rate independence.
- Linear dose-response over a wide range (up to several kilograys).
- Temperature stability under standard irradiation and storage conditions.

Comparison to Other Dosimetry Systems

Compared to other dosimetry systems such as ionization chambers, TLDs, or radiochromic film, alanine dosimetry offers excellent linearity, long-term stability, non-destructive readout, and minimal dependence on environmental conditions. However, due to the complexity and cost of ESR systems, as well as the required post-irradiation stabilization time, alanine dosimetry is less suited for routine clinical workflows. Instead, alanine pellets are frequently used in reference laboratories for dose audits, benchmarking, and the validation of clinical dosimetry systems [17].

2.3 Radiochromic Film Dosimetry

Radiochromic film (RCF) dosimetry has become a widely used technique in modern radiotherapy quality assurance due to its high spatial resolution, tissue-equivalence, and suitability for 2D dose verification. GafChromic films such as EBT3 and EBT 4 are among the most commonly used models in clinical and research applications. These films contain a sensitive polymer layer that undergoes radiation-induced polymerization, leading to a visible color change that can be quantified through optical density (OD) measurements.

Film Readout and Color Channels

Modern RCF dosimetry systems use flatbed color scanners to acquire digital images of irradiated films. These scanners operate in 48-bit color mode, capturing the red, green, and blue (RGB) channels separately. Each channel corresponds to a distinct region of the film's absorption spectrum, with absorption peaks typically around 636 nm (red), 585 nm (green), and 420 nm (blue)[17].

Historically, film dosimetry was performed using only the red channel due to its higher sensitivity at clinically relevant dose levels (<10 Gy). However, relying on a single channel has limitations: it does not account for variations in film thickness, scanner non-uniformities, or environmental factors such as humidity and temperature.

To overcome these limitations, triple-channel dosimetry was introduced. This method, originally developed by Micke, Lewis, and Yu, analyzes all three RGB channels simultaneously, allowing separation of dose-dependent and dose-independent components. This leads to improved accuracy, homogeneity, and resilience to artifacts such as lateral response variation and film non-uniformity [18], [19].

Film Response and Calibration

The dosimetric response of RCFs is nonlinear, particularly at very low and very high dose regions. As a result, calibration is typically performed using rational functions that accurately model the dose–OD relationship across the full dynamic range. The optical density is calculated as [20]:

$$\mathrm{OD} = \log_{10}\left(\frac{I_0}{I}\right), \tag{2.2}$$

where I_0 is the light intensity without the film, and I is the transmitted intensity through the irradiated film.

Due to the high spatial resolution of RCFs—on the order of microns—they are ideal for small field dosimetry and steep gradient regions such as in intensity-modulated radiation therapy (IMRT), volumetric modulated arc therapy (VMAT), and stereotactic radiosurgery (SRS). However, accurate dosimetry also depends on minimizing artifacts like Newton rings, which can occur due to interference patterns between the film and scanner glass. To eliminate this issue, silica particles are incorporated into the polyester substrate of EBT3 films [17].

2.4 External Beam Radiotherapy (EBRT)

Linear accelerators are the most widely used radiation sources for external beam radiotherapy (EBRT), providing high-energy photon or electron beams for patient treatment. Unlike radioactive sources, which rely on the decay of unstable nuclei, LINACs generate radiation on demand by accelerating electrons using electromagnetic fields and subsequently converting their kinetic energy into therapeutic radiation [21].

LINACs operate by accelerating charged particles, such as electrons, along a straight trajectory using time-varying electric fields. Unlike circular accelerators, LINACs avoid the need for magnetic deflection, simplifying beam optics and eliminating energy losses due to synchrotron radiation [22].

The core process begins in the *injection system*, where electrons are produced by thermionic emission from a heated cathode within the electron gun. The emitted electrons are focused into a narrow beam by a focusing electrode and are initially accelerated toward a perforated anode, through which they enter the accelerating structure [21].

Acceleration occurs within the *accelerating waveguide*, a cylindrical structure containing a series of resonant cavities. High-frequency microwave power is delivered into the waveguide by the *RF power generation system*, which consists of either a magnetron or a klystron depending on the beam energy requirements [21]. These microwaves create an oscillating electromagnetic field that interacts with the injected electron bunches, continuously accelerating them as they travel through the waveguide [21], [22].

As the electrons gain energy, the length of each drift tube or cavity increases progressively to accommodate their increasing velocity, ensuring that the RF fields remain synchronized with the particles' transit time, a principle known as phase stability [22]. This synchronization is critical to ensure efficient energy transfer and continuous acceleration.

During acceleration, beam stability is maintained through *beam steering and focusing systems*, including solenoid coils for focusing and steering coils to correct for beam trajectory deviations. The entire acceleration process takes place under ultra-high vacuum to minimize electron scattering [21].

Upon exiting the accelerating structure, the high-energy electron beam must be aligned with the treatment beam axis. As the waveguide is typically mounted horizontally within the gantry for space considerations, a *bending system* employing 90° or 270° bending magnets redirects the beam vertically while minimizing energy spread and focal spot enlargement [21].

Finally, the accelerated electrons can either directly form an electron treatment beam or strike a high-Z target (e.g. tungsten), producing bremsstrahlung X-rays for photon treatments. These therapeutic beams are then shaped, monitored, and delivered to the patient using complex collimation and beam monitoring systems [21].

An essential advantage of LINACs lies in their ability to produce continuous and controllable beams without the limitations of magnetic focusing inherent to circular accelerators. Moreover, linacs are free from relativistic phase slippage, making them particularly well-suited for high-energy electron acceleration where relativistic effects dominate even at relatively low energies [22].

A schematic representation of the operational principle of a linear accelerator is shown in Figure 2.3.

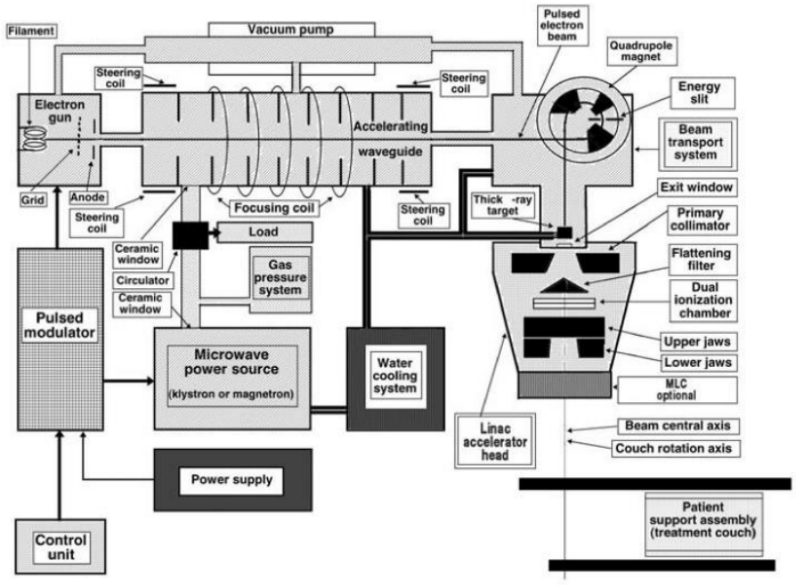

Figure 2.3: Working principle of a linear accelerator [21].

2.5 Principles of Brachytherapy

Brachytherapy is a form of internal radiotherapy in which sealed radioactive sources are placed directly within or in close proximity to the target tissue. Unlike EBRT, where radiation is delivered from a distance, brachytherapy allows for highly localized dose delivery, exploiting the rapid dose fall-off with distance due to photon attenuation and scattering [23].

The fundamental concept of brachytherapy is to place the radiation source as close as possible to the tumor, maximizing the dose to malignant tissue while sparing surrounding healthy OARs. This proximity allows for steep dose gradients, enabling highly conformal dose distributions even in anatomically complex regions [23].

Radiation in brachytherapy can be delivered using various radionuclides or electronic sources. Traditional isotopic sources include ^{192}Ir, ^{137}Cs, ^{125}I, and ^{103}Pd, which emit gamma rays of different energies. More recently, miniature X-ray tubes have been introduced in electronic brachytherapy systems, producing low-energy X-rays without the use of radioactive isotopes [23].

Depending on the energy, activity, and delivery technique, brachytherapy can be categorized into low-dose rate (LDR), high-dose rate (HDR), and pulsed-dose rate (PDR) treatments. In LDR brachytherapy, sources continuously emit radiation over extended periods, often via permanent implants ("seeds"). In contrast, HDR brachytherapy utilizes highly active sources that deliver the prescribed dose in short treatment sessions, often with remote afterloading systems that improve radiation safety for healthcare staff [23].

The dosimetric characteristics of brachytherapy are described using formalisms such as the AAPM TG-43 protocol, which defines parameters like air kerma strength, dose rate constant, radial dose function, and anisotropy function. These parameters account for the source geometry, photon attenuation, scattering, and tissue heterogeneity, enabling

accurate dose calculation and treatment planning [23].

2.5.1 HDR Brachytherapy

In HDR brachytherapy, a single highly active radioactive source is temporarily introduced into pre-positioned applicators or catheters located within or adjacent to the tumor volume. The most commonly used isotopes for HDR brachytherapy include ^{192}Ir and occasionally ^{60}Co, which emit gamma photons with mean energies of approximately 300–400 keV [23]. Due to the high activity of the source, the prescribed dose can be delivered within a few minutes, allowing for outpatient procedures and reducing overall treatment times.

The source is remotely controlled by an afterloading system, which automatically transfers the active source into the applicator via transfer tubes and positions it at specific dwell positions along the treatment channel. The dwell time at each position is individually optimized during treatment planning to achieve the desired dose distribution and to minimize radiation exposure to adjacent organs at risk [23].

HDR brachytherapy offers several advantages, such as highly conformal dose distributions through dwell time modulation, enhanced radiation safety for medical staff due to remote source handling, and broad applicability across various tumor sites. The steep dose gradients achieved enable effective tumor dose escalation while maintaining acceptable toxicity profiles for surrounding normal tissues [23].

2.5.2 Electronic Brachytherapy

Electronic brachytherapy (eBT) utilizes miniaturized X-ray tubes instead of sealed radioactive sources to generate low-energy X-rays, typically in the range of 20 – 50keV, directly at the treatment site [23]. As the radiation is produced on demand, electronic brachytherapy systems eliminate the need for radioactive isotope storage, handling, and disposal, significantly simplifying logistical and radioprotection aspects of treatment delivery.

Common commercial systems include the Xoft Axxent, Intrabeam (Zeiss), and Esteya (Elekta) devices [23]. Due to their low photon energy, electronic brachytherapy systems produce very steep dose gradients and limited tissue penetration compared to conventional HDR brachytherapy. This makes eBT particularly suitable for superficial lesions, intraoperative radiotherapy, and certain intracavitary applications.

However, the distinct dosimetric characteristics of eBT require careful consideration regarding dose uniformity, radiobiological effects, and treatment planning optimization to ensure adequate target coverage while preserving surrounding healthy tissues [23].

Chapter 3

Materials

3.1 HYPERSCINT-Research Platform 200 OFS

3.1.1 Optical Fiber Scintillator

The HYPERSCINT Research Platform 200, developed by Medscint Inc., is a fiber-based dosimetry system designed for high-precision dose measurements in radiotherapy research. Medscint is a Canadian company headquartered in Québec, specializing in the development of scintillation dosimetry technologies for medical physics and radiation oncology. According to the company, its mission is "to push the limits of innovation in radiotherapy and facilitate the work of medical physicists and researchers in radiation oncology worldwide" [16], [24]. Figure 3.2 shows the HS-RP200 optical fiber scintillator system manufactured by Medscint.

Figure 3.1: HS-RP200 [3].

The HYPERSCINT Research Platform 200 applies the scintillation mechanism described in Section 2.1, utilizing a plastic scintillation element coupled to a long optical fiber to enable remote, real-time detection of radiation-induced optical signals. A spectral and dose calibration is applied. In the absence of an external absolute detector to perform dose calibration, dosimetry with the HS-RP200 is conducted on a relative basis.

Scintillator Composition and Mechanism

The active sensing element consists of a proprietary polystyrene-based plastic scintillator, engineered to be near water-equivalent in density and atomic composition. The polystyrene scintillator emits visible light in the blue region (typically around 423 nm) following energy deposition by ionizing radiation. The light yield is proportional to the energy deposited by charged particles, assuming a linear scintillation efficiency, which is valid above approximately 100 keV electron energy — the dominant regime in MV photon and electron beams [5].

This light is transmitted via polymethyl methacrylate (PMMA)-core optical fibers to the optical reader, which spectrally resolves and quantifies the scintillation signal using a cooled spectrometer.

Background Signal Correction and Cerenkov Removal

As discussed in Section 2.1, plastic optical fibers inherently produce unwanted background signals, primarily due to Cerenkov radiation and fiber-induced fluorescence. To mitigate this stem effect, the HS-RP200 system employs a five-component spectral calibration protocol. This method enables the accurate subtraction of non-dosimetric light contributions, thereby isolating the scintillation signal that is proportional to the absorbed dose [3].

Water-Equivalence

A critical advantage of plastic scintillators is their near water-equivalence. The mass energy-absorption coefficients, mass collision stopping powers, and scattering properties of the polystyrene-based scintillator approximate those of water across the clinical energy range, typically within a few percent [5].

Comparison to Other Dosimetric Systems

Compared to other dosimetry systems such as ICs, TLDs, radiochromic films, and diodes, OFSs like the HS-RP200 exhibit distinct characteristics. Due to their near water-equivalence, OFS systems minimize the need for correction factors related to mass energy-absorption differences. The small active volume allows high spatial resolution, which is particularly beneficial for small field dosimetry and stereotactic applications. In contrast to passive systems such as TLDs and films, OFS detectors provide immediate real-time readout, without requiring post-irradiation processing. Furthermore, unlike some semiconductor diodes, OFS systems generally exhibit negligible angular and dose-rate dependence, and are less sensitive to environmental conditions such as temperature and humidity variations [5, 6].

3.1.2 Five-Component Spectral Calibration of the HS-RP200

The five-component spectral calibration implemented in the HS-RP200 system is designed to isolate the true scintillation signal from various contaminating optical signals that arise during irradiation. These background signals include Cerenkov radiation generated in the optical fiber, fluorescence of the fiber material, and a constant electronic or thermal offset.

Rather than attempting to suppress these contributions physically, the system employs a hyperspectral decomposition technique, whereby the complete optical spectrum acquired by the reader is mathematically decomposed into five distinct components. This process allows real-time extraction of the scintillation signal based solely on its spectral shape, even when overlapped by other sources of light. This calibration method was originally developed and implemented by Medscint as a proprietary solution to overcome the stem effect and enhance the accuracy of plastic scintillation dosimetry.

Spectral Decomposition Model

During calibration, the system collects the full emission spectrum under five controlled irradiation conditions, each isolating one of the following spectral components:

1. Scintillation: light produced exclusively in the plastic scintillator.
2. Fluorescence: light emitted by the polymer optical fiber itself due to excitation by X-rays.
3. Cerenkov I & II: forward and backward Cerenkov radiation generated in the fiber at short source distances.
4. Cerenkov III & IV: same as above, but with the scintillator further from the irradiation field, enhancing spatial separation.
5. Offset: a baseline correction term to account for background signal in the absence of irradiation.

Figure 3.2 shows the individual spectral components involved in the signal decomposition.

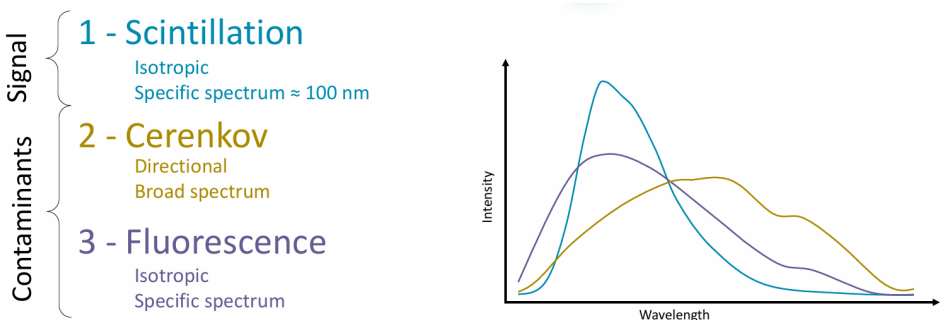

Figure 3.2: Spectral components contributing to the scintillation signal [25].

Mathematically, the spectrum acquired during measurement S_{measured} can be represented as a linear combination:

$$S_{\text{measured}} = \sum_{i=1}^{5} \alpha_i \cdot S_i$$

where each S_i is one of the five calibration spectra, and α_i the corresponding weight. The scintillation coefficient α_{scint} is the one used for dose determination.

This conceptual model follows standard linear unmixing techniques commonly applied in hyperspectral detection [6].

Purposes and Advantages

Traditional plastic scintillator dosimetry systems suffer from stem effect contamination, where light is generated in the optical fiber due to Cerenkov or fluorescent processes. Earlier systems required shielding, filtering, or dual detectors to mitigate this. The five-component method used in the HS-RP200 provides several key advantages:

- Spectral selectivity: each component has a unique spectral fingerprint, allowing accurate separation without physical shielding.
- Robustness to setup changes: once calibrated, the system can tolerate minor changes in position or angle.
- Multi-channel compatibility[1]: each scintillator channel can be independently calibrated and corrected, enabling simultaneous measurements.

The method builds upon prior work showing that plastic scintillators exhibit highly reproducible and energy-independent emission spectra when irradiated with high-energy photons or electrons [5], [6].

Practical Calibration Considerations

According to [3]:

- The spectral calibration must be performed with SNR greater than 300 for scintillation and greater than 100 for fluorescence.
- The detector must remain connected after calibration to ensure validity.
- Recalibration is recommended every 3 months (spectral) or daily (dose).
- For the Cerenkov measurements, different gantry angles (e.g., 45° and 315°) are used to enhance directional components.

Although these steps are described procedurally in [3], the underlying mathematical decomposition and principles are not fully detailed. These concepts align with generalized hyperspectral signal processing strategies used in optical physics and dosimetry.

The implementation of the calibration procedure for this study is further described in Section 4.1.1.

3.2 Alanine Dosimetry

Alanine dosimetry is used in this study as reference method for assessing the accuracy of the HS-RP200, as it is an absolute dosimeter.

[1] Although the HS-RP200 supports multiple channels, only a single-channel configuration was used in this study.

Alanine Composition

In practice, alanine pellets are small cylindrical solids, typically composed of ∼91% L-α-alanine and ∼9% paraffin as a binder. After irradiation, a post-exposure stabilization period of 3 - 5 days is required to allow the radical concentration to stabilize. This delay is a key limitation of the technique, as it precludes real-time measurements [17].

Alanine Dosimeter Readout Using EPR Spectroscopy

Following irradiation, alanine dosimeters are read out using EPR spectroscopy, which detects the stable radiation-induced free radicals formed within the alanine matrix. The concentration of these unpaired electrons is directly proportional to the absorbed dose.

The EPR readout process is based on the Zeeman effect, where the magnetic moments of the unpaired electrons split into distinct energy levels under the influence of a static magnetic field. By applying radiofrequency (RF) electromagnetic radiation, transitions between these spin states are induced when the resonance condition is met. Typically, the magnetic field is gradually swept while the RF frequency is held constant, allowing identification of the resonance field for maximal absorption [17].

Because the EPR absorption signal is inherently weak, phase-sensitive detection is employed. In this approach, a small modulation is added to the magnetic field, and the first derivative of the absorption spectrum is measured. This technique significantly enhances the SNR and improves measurement sensitivity [17].

Measurement Process and Correction

To ensure reproducibility and account for potential drift in spectrometer sensitivity or magnetic field stability, a reference material—such as a chromium-doped sample or a ruby crystal—is placed near the alanine sample during readout. The EPR signal from the alanine is then normalized to that of the reference, ensuring reproducible and stable measurements over time [17].

Signal Analysis and Calibration

Once stabilized, the pellets are inserted into the EPR spectrometer for signal acquisition and analysis. The measured spectrum is fitted to base functions representing the alanine and reference signals. This fitting yields a dose-normalized amplitude A_D^b, which can be interpreted using a linear calibration curve [26]:

$$A_D^b = p_1 \cdot D + p_0, \tag{3.1}$$

where A_D^b is the normalized EPR signal, D is the absorbed dose, and p_0, p_1 are calibration constants.

Calibration is typically performed using reference irradiations with ^{60}Co gamma rays. To evaluate detector response in different conditions (e.g. MV X-ray beams), the measured dose can be compared to the applied dose using the relative response r [26]:

$$r = \frac{D_{\text{calc}}}{D_{\text{applied}}}. \tag{3.2}$$

Experimental studies have shown that the relative response of alanine dosimeters in 8 MV and 16 MV photon beams is within 0.4% of the response to ^{60}Co [26].

3.3 Radiochromic Film Dosimetry

In this study, GafChromic EBT3 radiochromic films (Ashland Inc., USA) were used for two-dimensional dose measurements. Ashland Inc. is an American company specializing in the production of chemicals, plastics, and specialized materials and services, including GafChromic film dosimetry products [27]. The films consist of a symmetric three-layer structure with an active layer of approximately 30 μm, coated on both sides by 125 μm polyester substrates. The films were cut into pieces of appropriate size for irradiation and scanning, ensuring minimal edge artifacts. Batch-specific calibration was performed to account for potential manufacturing variations between film lots [17].

After irradiation, films were handled with care to avoid fingerprints, dust, scratches, or bending, all of which can introduce optical artifacts. Films were consistently positioned at the center of the scanner bed to minimize lateral response artifacts (LRA), and the same orientation (landscape or portrait) was maintained across all scans to prevent angular dependence effects [17]. Environmental factors such as temperature and humidity were controlled and documented throughout the measurements [17].

Radiochromic films continue to undergo post-irradiation polymerization for up to 24 hours. Therefore, all scans were performed at least 24 hours post-irradiation to ensure signal stabilization [28].

Scanning Procedure

Film scanning was performed using an Epson Expression 12000XL flatbed scanner (Seiko Epson Corporation, Japan), operated in transmission mode. Seiko Epson Corporation, headquartered in Suwa, Japan, is a manufacturer of printers, scanners, and computing equipment [29]. The scanner was controlled via the commercial software package FilmQA Pro (Ashland Inc., USA) [27]. Scanning was performed in 48-bit RGB color mode with all color correction features disabled [17].

To eliminate Newton rings—interference patterns caused by air gaps between the film and scanner glass—an anti-Newton ring glass plate was placed on top of the films during scanning, ensuring uniform contact [17].

Calibration and Data Analysis

All film analysis and dose reconstruction were performed using FilmQA Pro software. The multichannel dosimetry algorithm implemented in FilmQA Pro utilizes information from all three color channels (red, green, and blue) to separate dose-dependent and dose-independent components, thereby minimizing artifacts such as lateral response variations and non-uniform film thickness [18, 19].

The pixel values from the scanned images were first converted to optical density using formula 2.2.

Calibration curves were generated by irradiating calibration films with known dose levels covering the full clinical dose range. A rational function was fitted to the calibration data to describe the nonlinear dose-response relationship of the films [20]. The same scanner and scanning conditions were used for both calibration and measurement films to avoid scan-to-scan variability [30], [31].

Lateral response corrections, as well as spatial non-uniformity corrections, were applied during dose reconstruction to ensure consistent and accurate dose evaluation across the entire film surface [31].

3.4 Varian TrueBeam Linear Accelerator

Varian, a Siemens Healthineers company headquartered in Palo Alto, United States, develops and manufactures innovative technologies and solutions used by healthcare providers worldwide to treat millions of patients annually [32]. Among its product portfolio is the Varian TrueBeam linear accelerator, which was utilized as one of the modalities in this study. Figure 3.3 shows the Varian TrueBeam linear accelerator.

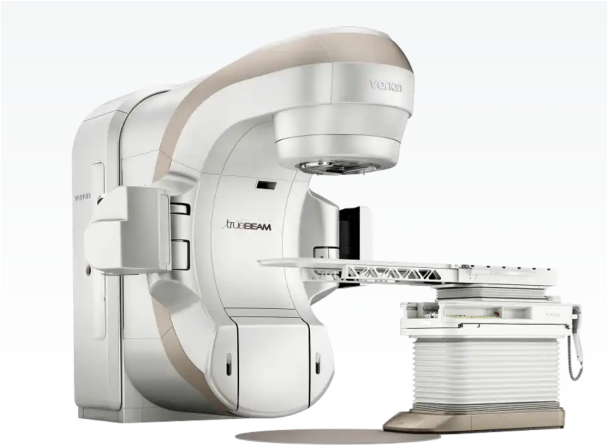

Figure 3.3: Varian Truebeam linear accelerator [32].

System Overview

The Varian TrueBeam linear accelerator is a modern radiotherapy platform capable of delivering both photon and electron beams with high precision. Introduced into clinical practice in 2010, the system supports a wide range of advanced treatment techniques including IMRT, VMAT, Stereotactic Body Radiation Therapy (SBRT), and SRS [33], [34].

Beam Energies and Flattening Filter Free Mode

The TrueBeam system provides multiple photon and electron energies. Photon beam energies include 6 MV, 10 MV, and 15 MV, while electron beam energies range from 6 MeV to 22 MeV [33]. The system also offers Flattening Filter Free (FFF) photon beams,

which allow for significantly higher dose rates (up to 2400 Monitor Units (MU)/min for 10 MV FFF) by removing the flattening filter from the beam path. The FFF mode reduces treatment times and facilitates improved motion management for certain clinical applications [34].

Multileaf Collimator

Beam shaping is performed using a high-resolution multileaf collimator (MLC) consisting of 120 independently controlled tungsten leaves. The inner 40 leaf pairs have a projected width of 5 mm at isocenter, enabling the delivery of highly conformal dose distributions for advanced techniques such as IMRT and VMAT [33], [35].

Image Guidance and Verification

The TrueBeam system includes integrated image guidance capabilities through its kilovoltage (kV) on-board imager (OBI) and MV portal imaging panel. Available image guidance techniques include orthogonal kV imaging, cone-beam computed tomography (CBCT), and MV portal imaging, all of which enable precise patient positioning and verification of internal anatomy prior to treatment [34], [36].

Treatment Planning Integration

The TrueBeam is fully integrated with the Eclipse Treatment Planning System (Varian Medical Systems), allowing seamless transfer of treatment plans and delivery parameters. Complex delivery techniques such as VMAT and dynamic MLC-based IMRT are executed automatically according to the pre-optimized plan [33], [37].

3.5 Varian Bravos HDR Afterloader

In addition to the Varian TrueBeam linear accelerator, Varian also manufactures brachytherapy systems, including the Varian Bravos HDR afterloader. This is one of their systems dedicated to HDR brachytherapy and was utilized in this study [32], [38]. Figure 3.4 shows the Varian Bravos HDR Afterloader.

Figure 3.4: Varian Bravos HDR Afterloader [32].

System Description

The Varian Bravos is a modern remote afterloader designed for the safe and precise delivery of HDR brachytherapy. The system operates with a high-activity ^{192}Ir source, typically up to 370 GBq, housed within a shielded source container [39], [40]. A motorized cable drive mechanism moves the source through flexible transfer tubes connected to applicators.

The Bravos supports up to 40 independent channels, allowing for complex treatment geometries and multiple catheter setups. The system incorporates real-time source tracking, automated safety checks for system integrity, source verification, and channel patency detection. Full integration with the Varian BrachyVision TPS enables optimized dwell time calculations, plan transfer, and automated treatment delivery [39], [40].

Operational Workflow

The general HDR brachytherapy workflow using the Bravos system includes the following steps [23]:

1. **Applicator Insertion:** A suitable applicator (e.g. vaginal cylinder, interstitial needle array) is positioned within or near the treatment region.
2. **Imaging:** CT or Magnetic Resonance Imaging (MRI) scans are acquired with the applicator in place to visualize anatomy and define the clinical target volume (CTV) and OARs.
3. **Treatment Planning:** Based on the acquired imaging data, a treatment plan is generated in BrachyVision TPS. Dwell positions and times are optimized to meet the prescribed dose constraints.
4. **Plan Export and Delivery:** The finalized treatment plan is transferred to the Bravos afterloader. Following patient and applicator setup verification, the system initiates source transport.
5. **Source Delivery:** The ^{192}Ir source is advanced through indexed transfer tubes into the applicator channels. The source stops at each programmed dwell position for the prescribed dwell time.
6. **Retrieval and Verification:** After completing the dwell sequence, the source is retracted into its shielded housing. A post-treatment verification is performed to confirm correct delivery.

Throughout the treatment, safety interlocks and emergency retraction functions remain active to ensure patient and staff safety.

Dosimetry and Treatment Planning

Dose calculations for HDR brachytherapy treatments with the Bravos system follow the AAPM TG-43 formalism [41]. The dose distribution is computed using standardized source parameters, including the dose-rate constant Λ, radial dose function $g(r)$, and anisotropy function $F(r, \theta)$, all specific to the ^{192}Ir source [23].

The BrachyVision TPS incorporates these TG-43 parameters to generate the dose distributions and corresponding dose-volume histograms (DVHs) for both target volumes and OARs. Optimization algorithms adjust the dwell positions and times accordingly to achieve the prescribed dose coverage while minimizing dose to surrounding healthy tissues [39].

System Safety and QA

The Bravos afterloader includes multiple automated safety features and quality assurance mechanisms to ensure treatment accuracy and operational safety [39], [40]:

- **Real-time source position monitoring** to track the source location throughout treatment.
- **Daily automated system self-checks** to verify system readiness and source integrity.
- **Catheter patency verification** to detect potential channel obstructions prior to source deployment.
- **Emergency retraction system** allowing immediate withdrawal of the source in the event of system errors.
- **Remote diagnostics and service support** to minimize clinical downtime and maintain system reliability.

3.6 Axxent Xoft Electronic Brachytherapy System

The Axxent Xoft Electronic Brachytherapy System (iCAD Inc., USA) was used in this study as an alternative non-isotopic brachytherapy modality. Unlike conventional HDR systems utilizing radioactive sources such as ^{192}Ir, the Xoft system employs a miniaturized electronic X-ray tube operating at 50 kV to generate therapeutic radiation [42].

System Description

The Axxent system consists of several integrated components [42]:

- The **Controller**, which supplies high voltage and filament current to the X-ray source and controls the source movement via a digitally controlled pullback arm.
- The **X-ray Source 2.2**, a disposable, miniaturized X-ray tube mounted on a flexible catheter.
- A variety of **applicators**, including balloon applicators, vaginal cylinders, and surface applicators for intracavitary and superficial treatments.
- A closed-loop **cooling system** utilizing sterile water to dissipate heat generated during source operation.
- An integrated **vacuum pump** for evacuating the cooling fluid post-treatment.

The electronic source is advanced and retracted automatically along the applicator channel, pausing at preprogrammed dwell positions. Individual dwell times at each position allow the creation of highly conformal dose distributions [42].

Treatment Workflow

The general treatment workflow with the Axxent Xoft system includes [42]:

1. **Applicator Placement:** The appropriate applicator is inserted into or positioned adjacent to the treatment volume.
2. **Imaging and Planning:** CT or MRI imaging is performed with the applicator in place. Treatment planning is conducted in an external TPS, defining dwell positions and corresponding dwell times.
3. **Source Calibration:** The air kerma strength of the X-ray source is measured prior to clinical use using a well chamber and electrometer, following TG-43 protocol guidelines.
4. **Treatment Delivery:** The treatment plan is transferred to the controller, which moves the source to each programmed dwell position for dose delivery.
5. **Verification and Logging:** Following treatment completion, the source is retracted into its shielded housing and all delivery data are automatically recorded.

Dosimetry and Treatment Planning

Although the Axxent system utilizes electronic X-rays rather than radioactive isotopes, dose calculations follow the AAPM TG-43 formalism. The treatment planning system applies source-specific dosimetric parameters, including:

- Air kerma strength (S_k),
- Radial dose function ($g(r)$),
- Anisotropy function ($F(r, \theta)$),
- Dose-rate constant (Λ).

These parameters have been validated for the 50 kV source, both with and without titanium filtration [42].

System Safety and Technical Specifications

The Axxent Xoft system incorporates several operational features and safety mechanisms [42]:

- Fully automated source positioning and pullback control.
- Real-time monitoring and safety interlocks.
- No handling or storage of radioactive isotopes required.
- Compact, mobile system design allowing flexible room use.

- Total source lifetime limited to 750 minutes.

The relatively low photon energy (50 kV) limits the penetration depth, making the system primarily suited for superficial and intracavitary targets rather than deep-seated lesions [42].

3.7 Precision X-Ray MultiRad 225

Precision X-Ray Inc., headquartered in Connecticut, USA, is an American company specializing in the development and innovation of X-ray technologies for biomedical research and various industrial applications. According to the company, its mission is "to inspire new and daring research in the global fight against disease as well as other critical multi-industry applications in a wide array of emerging fields" [43]. Among its product portfolio is the MultiRad 225, a preclinical X-ray cabinet system. Figure 3.5 shows the MultiRad 225.

Figure 3.5: MultiRad 225 [43].

System Description and Technical Specifications

The MultiRad 225 is a self-contained, cabinet-based X-ray irradiation system used for preclinical and radiobiological applications. The system employs a high-voltage X-ray generator delivering photon beams up to 225 kVp without the use of radionuclide sources [11]. The unit includes an integrated 225 kV X-ray tube, operating at tube voltages from 20 to 225 kV and currents between 0.1 and 30 mA, with a maximum tube power of 4 kW. The beam exits through a 0.8 mm beryllium window at a 40° divergence angle [11].

The irradiation field is defined by the motorized specimen shelf position and optional collimators. An integrated dosimeter and a rotating stage ensure real-time dose monitoring and uniform dose delivery [44]. The system operates at 50% duty cycle when ambient room temperature remains below 23°C [11].

Software and Operational Modes

System operation is managed through the Precision Rad software interface on a touch-screen PC. Available modes include [11]:

- **Manual Mode:** user-defined exposure parameters.
- **ADC Program:** automatic dose delivery using the integrated dosimeter.
- **Dose Mapping:** spatial dose distribution measurement.

A daily warm-up procedure is required prior to irradiation: 20 minutes if used recently or 60 minutes after extended inactivity [11]. Real-time feedback includes dose rate, accumulated dose, and system status.

Dosimetry and Calibration

The built-in ionization chamber at the center of the rotating stage provides real-time dosimetry. Calibration follows AAPM TG-61 protocol, suitable for low-energy X-ray beams between 40–300 kV [44].

Correction factors applied include [44]:

- Temperature-pressure correction (P_{TP}),
- Ion recombination correction (P_{ion}),
- Polarity correction (P_{pol}),
- Electrometer calibration correction (P_{elec}),
- Backscatter factor (B_w),
- Mass energy-absorption coefficient ratio.

Regular verification is performed using external reference ionization chambers (e.g. Farmer-type) to validate dose output, particularly when additional filtration is applied (e.g. 0.3 mm Cu or 2 mm Al).

Safety Features

The MultiRad 225 incorporates multiple safety interlocks [44]:

- Door interlocks preventing exposure when open,
- Emergency stop function and X-ray ON indicators,
- Cooling system interlocks,
- Software-integrated error detection and logging.

Radiation leakage must not exceed 1 μSv/h at 10 cm distance during operation, in accordance with IEC 61010 and 21 CFR 1020.40 standards.

Chapter 4

Methodology

This chapter outlines the experimental procedures used to evaluate the performance of the OFS under various irradiation conditions. The methodology is divided according to the irradiation modality and describes in detail the calibration steps, measurement setups, and test procedures used for assessing reproducibility, linearity, accuracy and energy dependence.

Four different irradiation systems were investigated in this study: the Varian Truebeam linear accelerator (6 MV), the Varian Bravos afterloader (HDR brachytherapy), the Axxent Xoft system (electronic brachytherapy), and the Precision MultiRad225 system. Each modality required a distinct experimental setup, adapted to the characteristics and constraints of the respective irradiation system.

4.1 Varian Truebeam Linear Accelerator (6 MV)

All measurements were performed using 6 MV photon beams under identical conditions to ensure comparability of the results. Prior to the execution of these measurements, calibration of the OFS was required. The system necessitates a five-component calibration, comprising scintillation, fluorescence, two distinct Cerenkov spectra, and an offset spectrum [3]. For each of the Cerenkov components, two separate spectral acquisition measurements are necessary. The details of this calibration protocol are thoroughly outlined in the HS-RP200 manual [3].

4.1.1 Spectral Calibration of HS-RP200

Scintillation

The calibration process commenced with the scintillation component. To this end, the LINAC kV imager was activated, and the OFS was affixed to the center of the output window, as illustrated in Figure 4.1.

According to the manual, the kV imager should operate in continuous mode with the maximum possible output, without any filters or beam-hardening devices that could attenuate the beam. The measurement was initiated by pressing the start button in the

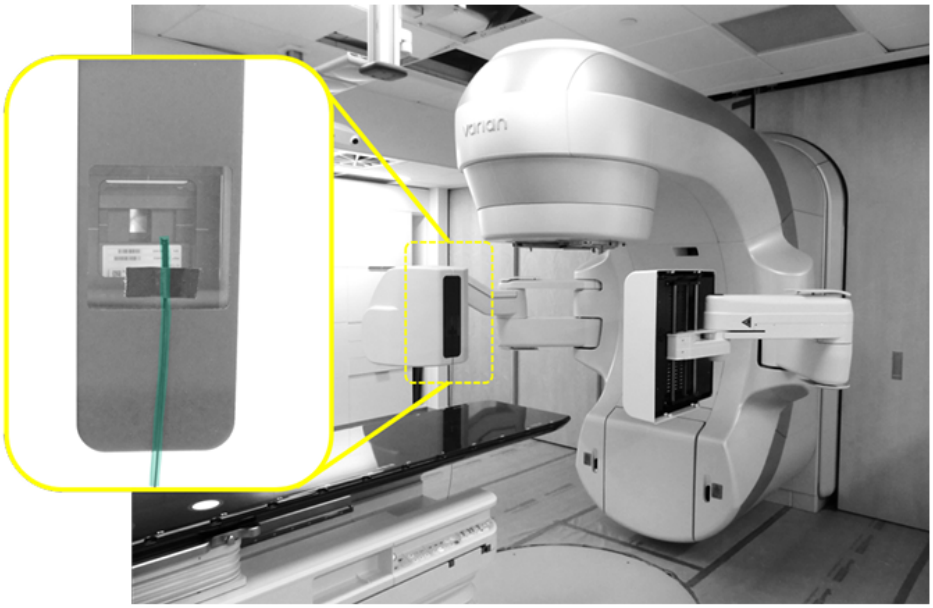

Figure 4.1: Example of the scintillation calibration component of Varian Truebeam LINAC [3].

HYPERDOSE RP software, prompting the OFS to begin acquisition. The OFS was irradiated using the kV imager until the SNR exceeded 300. At that point, the measurement was terminated via the HYPERDOSE RP software.

Fluorescence

The second step in the calibration procedure involves the fluorescence component. Six loops of the OFS, each with a diameter of 12 cm, were formed and affixed to the output window of the Varian TrueBeam LINAC's kV imager. The setup for this calibration component is depicted in Figure 4.2.

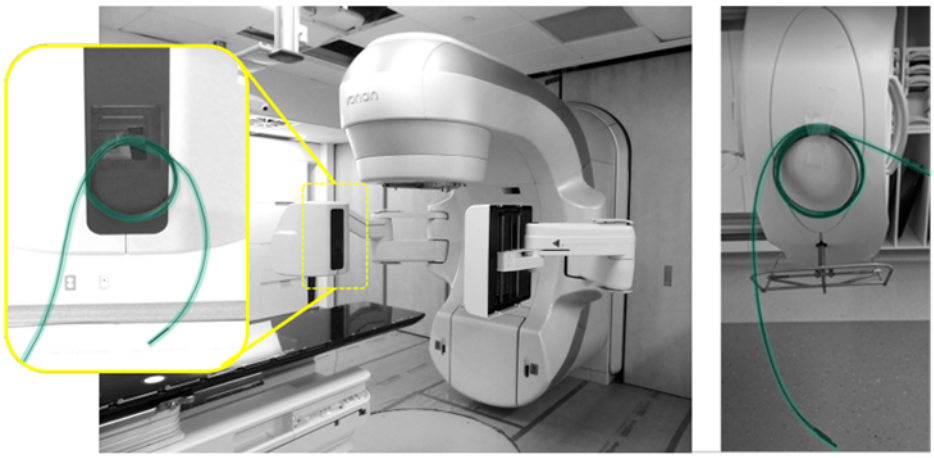

Figure 4.2: Example of fluorescence calibration of Varian Truebeam LINAC [3].

The procedure followed was analogous to that of the scintillation calibration, with the exception of the SNR requirement: for the fluorescence component, an SNR threshold of 100 is sufficient, rather than 300. As the subsequent calibration steps do not require use

of the kV imager, it can be returned to its standard position thereafter.

Cerenkov I & II

After completing the fluorescence calibration, the procedure continued with the spectral acquisition for the Cerenkov components. The Cerenkov components of the calibration procedure require either a water phantom tank or a solid water slab. In this experiment, a solid water slab with a thickness of 5 cm was used. For this part of the calibration, the OFS was positioned approximately 0.5 m from the center of the radiation field, with the source-to-surface distance (SSD) set to 100 cm. It is essential that only the central portion of the fiber is irradiated, ensuring that sections of the fiber running laterally through the slab are not exposed to the beam.

The distinction between the Cerenkov I and Cerenkov II components lies in the gantry rotation angle. For the Cerenkov I component, the gantry angle was set to 45°, while for the Cerenkov II component, it was adjusted to 315°. Once the setup was complete, the fiber was irradiated using a 6 MV photon beam. The calibration was performed with a dose of 500 MU, delivered at a dose rate of 600 MU/min, with the MLC in an open configuration. Recording was initiated and terminated via the HYPERDOSE RP software. The full prescribed setup for all Cerenkov calibration components is illustrated in Figure 4.3.

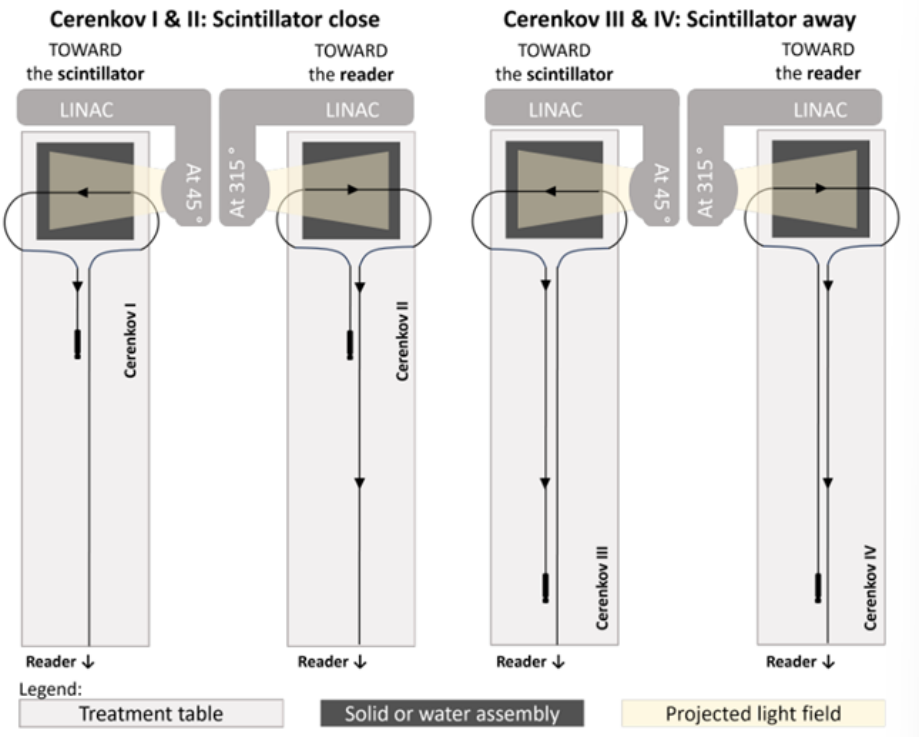

Figure 4.3: Schematic overview of Cerenkov component of five component calibration [3].

Figure 4.4 presents the experimental configuration of these components as implemented at Maastro.

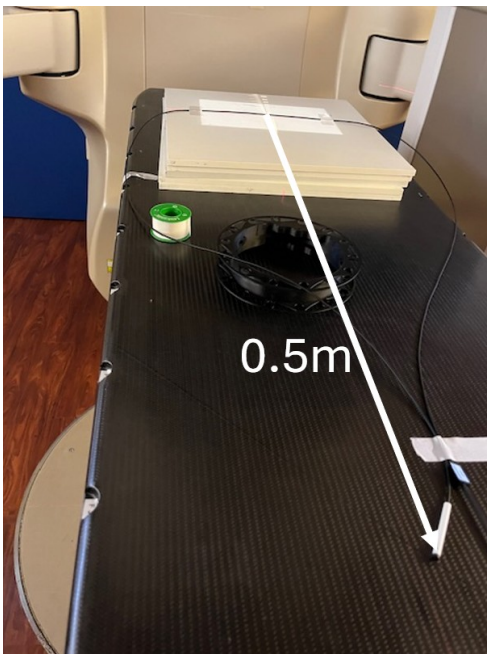

Figure 4.4: Experimental setup for Cerenkov I & II calibration.

Once both recordings—one for Cerenkov I at a gantry angle of 45°, and one for Cerenkov II at 315°—have been completed, the calibration procedure proceeds to the next steps.

Cerenkov III & IV

These steps are nearly identical to those described for the Cerenkov I and II components. The sole distinction lies in the positioning of the OFS end, which is placed at a distance of 1.5 m from the center of the radiation field, in contrast to the 0.5 m distance used for the Cerenkov I and II calibrations. The prescribed setup is illustrated in Figure 4.3, while the experimental implementation of these measurements at Maastro is shown in Figure 4.5.

Dose Calibration

Following the completion of the five-component calibration, the final step in the setup procedure is the dose calibration. For this step, the protocol established at Maastro was followed. According to this protocol, a 10 cm solid water slab is placed beneath the scintillator to ensure adequate backscatter. The scintillator itself is positioned within a custom-designed slab that also accommodates four alanine pellets. On top of the scintillator, a 1.5 cm bolus slab is placed to complete the setup.

The SSD remained set at 100 cm, and the scintillator was irradiated with 200 MU using a 6 MV photon beam.

4.1.2 Measurement Series

Upon completion of this final calibration step, the measurements for reproducibility, linearity, and accuracy were initiated. For the reproducibility tests, the same setup as used in the dose calibration was maintained. This measurement was repeated ten times. To

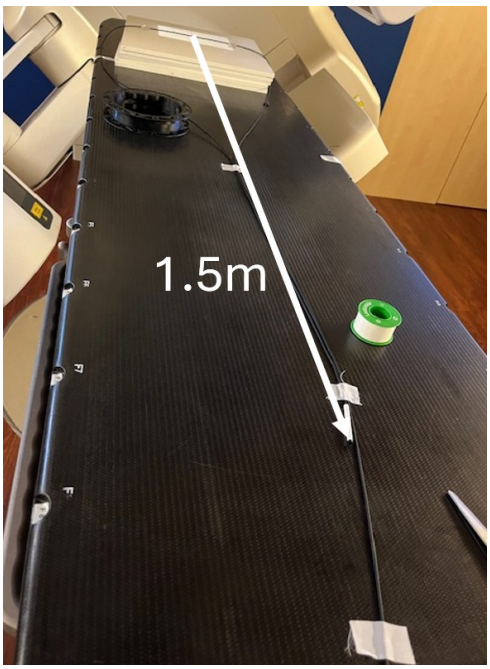

Figure 4.5: Experimental setup for Cerenkov III & IV calibration.

assess linearity, additional measurements were performed: three at 800 MU, three at 400 MU, and one at 1600 MU.

Finally, to evaluate the accuracy of the OFS, the eleven measurements—comprising the dose calibration and the ten reproducibility tests—were conducted using four alanine pellets inserted into the custom slab containing the scintillator. Figure 4.6 illustrates this slab with the scintillator and the four alanine pellets in place.

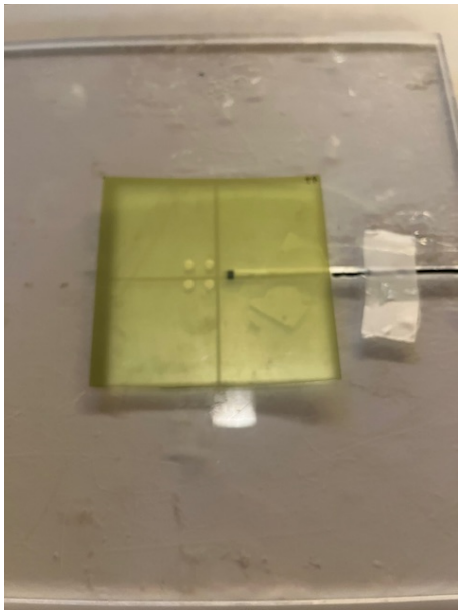

Figure 4.6: Slab with scintillator, four alanine pellets and film.

In two of the three measurements conducted at 800 MU, EBT3 films were included to obtain additional accuracy data. The films were placed on top of the OFS. The results of these measurements are discussed in Section 5.

4.2 Bravos Afterloader (HDR Brachytherapy)

The next modality investigated is the Bravos afterloader, used for HDR brachytherapy, as illustrated in Figure 4.7. The system utilizes a ^{192}Ir source with a mean photon energy of 390 keV and a source strength of 10.205 Ci.

Figure 4.7: Bravos afterloader.

4.2.1 HS-RP200 Calibration

Dose Calibration

For this modality, the five-component calibration previously performed with the 6 MV LINAC setup was reused. However, a new dose calibration was required due to the different source characteristics of the Bravos system. As the source itself cannot be modified, the delivered dose was adjusted by varying the dwell time. For the dose calibration, a dwell time of 50 seconds was used, resulting in a SNR of 4109.4.

Experimental Setup

The experimental setup is shown in Figure 4.8, and a detailed view of the phantom used is presented in Figure 4.9. The phantom was designed by Edward Ketels as part of his master's thesis [45]. In this configuration, the tip of the OFS was inserted 1 cm deeper into the phantom than the applicator and therefore also deeper than the source itself.

Figure 4.8: Experimental setup of the Bravos afterloader.

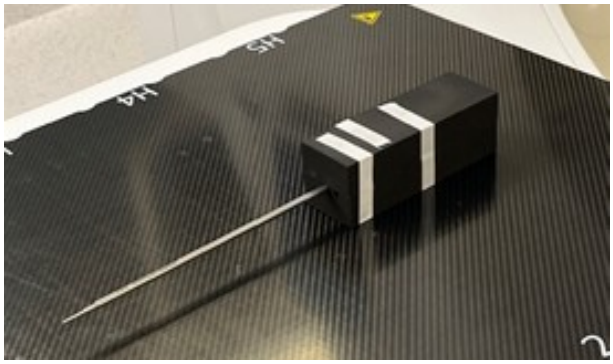

Figure 4.9: Custom phantom used for Bravos measurements [45].

To identify the dwell position that delivers the maximum dose, an initial irradiation was performed. This involved eleven dwell positions spaced 2 mm apart, each irradiated for 10 seconds. As expected, the highest dose was recorded when the source was positioned at the deepest dwell point within the applicator.

4.2.2 Measurements Series

Using this optimized configuration, the reproducibility, linearity, and accuracy of the OFS were evaluated for application in HDR brachytherapy with the Bravos afterloader.

To assess the reproducibility of the HS-RP200 under HDR brachytherapy conditions with the Bravos afterloader, ten repeated measurements were performed at a set dwell time of 50 seconds, corresponding to an expected dose of 183 cGy. The expected dose values were obtained from the TPS, which calculates the delivered dose based on the programmed dwell times and the source strength. These measurements were conducted with a single dwell position located at the tip of the applicator.

For the linearity evaluation, the dwell time was increased to 100 seconds, resulting in

an expected dose of 366 cGy. Five repeated measurements were performed under these conditions. Additional linearity points were acquired with dwell times of 40, 30, and 10 seconds, corresponding to expected doses of 146.4 cGy, 109.8 cGy, and 36.6 cGy, respectively. For the 40-second dwell time, five measurements were executed, while three repetitions were performed for both the 30-second and 10-second conditions.

Unlike the LINAC measurements, no EBT3 film or alanine dosimeters were used in this setup. Consequently, the accuracy of the OFS could not be evaluated using external reference dosimetry. Instead, the accuracy was assessed by comparing the measured OFS dose with the expected dose calculated by the TPS, taking into account uncertainties in source position and source strength.

4.3 Axxent Xoft (Electronic Brachytherapy)

The third modality examined is the Axxent Xoft system, which delivers electronic brachytherapy at an irradiation energy of 50 kVp [10]. The system is depicted in Figure 4.10.

Figure 4.10: Axxent Xoft.

4.3.1 Irradiation Parameters and Experimental Setup

Irradiation Settings and Dwell Time Correction

The irradiation time was determined based on the nominal dose rates specified in the Xoft system manual [42]. According to this reference, an output of 10,000 µGy/min corresponds to a dose rate of 0.73 Gy/min in water when using the 50 mm applicator cone. Since solid water slabs were used in this study, this conversion factor was adopted for all measurements. The system automatically adjusts the programmed dwell time to account for the actual calibration of the source. For instance, if the source has a calibration value of 13,548 µGy/min and the nominal dwell time is set to 100 seconds, the system applies a correction as follows:

$$100 \text{ s} \times \left(\frac{10\,000 \ \mu\text{Gy/min}}{13\,548 \ \mu\text{Gy/min}} \right) = 73.8 \text{ s}$$

This correction ensures that the delivered dose corresponds to the intended nominal dose rate despite variations in source strength.

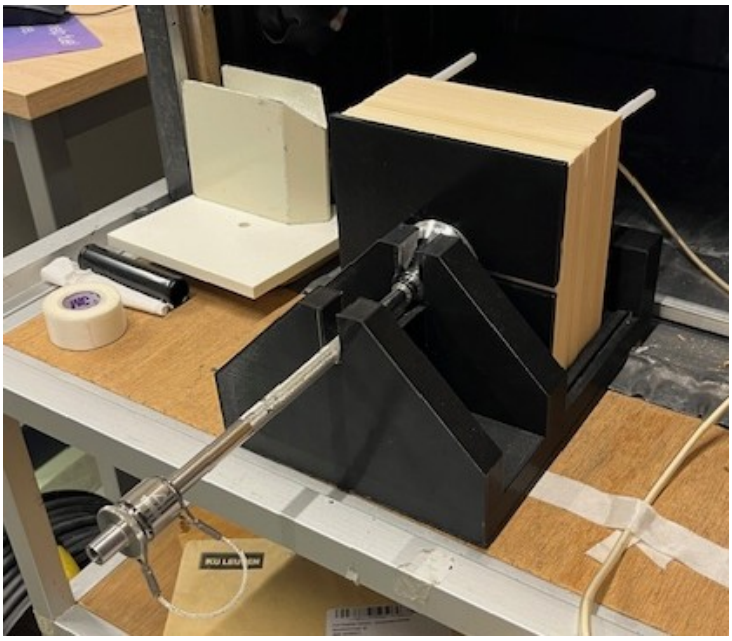

Figure 4.11: Phantom for Axxent Xoft measurements.

Experimental Setup

For these measurements, the scintillator was positioned within a custom-designed slab, which was placed adjacent to additional solid water slabs. The complete phantom setup is shown in Figure 4.11. Due to the difficulty of consistently positioning the source at the same depth within the applicator, an ionization chamber was used to correct for potential depth variations by normalizing the OFS signal. The applicator cone has a diameter of 50 mm. The full experimental setup is illustrated in Figure 4.12. During the measurements, zinc plates were added as shielding to cover the phantom.

4.3.2 Measurement Series

Using this configuration, experiments were carried out to assess the reproducibility of the OFS and to investigate the dependence of the measured signal on the depth of the OFS within the solid water slabs.

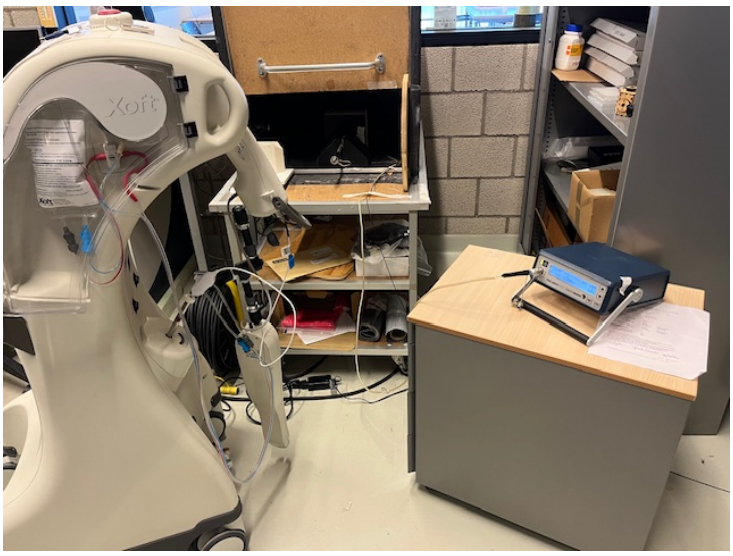

Figure 4.12: Full setup for Axxent Xoft measurements.

To evaluate reproducibility, ten measurements were performed with the OFS positioned adjacent to the applicator cone, where the highest dose is expected. The results of these measurements were normalized based on the depth of the source in the applicator, using the ionization chamber readings as a correction reference.

In addition, depth dependence of the OFS response was investigated by conducting three measurements with the scintillator placed at depths of 0.5 cm, 1.0 cm, and 1.5 cm within the solid water slabs.

4.4 MultiRad225

4.4.1 Experimental Setup

Initially, the fourth irradiation modality considered for this study was the X-RAD 225Cx Preclinical IGRT System. However, concerns arose regarding the mechanical limitations of the HS-RP200 OFS, particularly the risk of permanent damage when bent at a radius smaller than 6 cm. To assess the feasibility of using the OFS in this setup, preliminary tests were conducted using a metal wire to simulate the required bending path within the X-RAD 225Cx. These tests showed that the bending radius was insufficient, likely exceeding the safe limit of the fiber, and thus the X-RAD 225Cx was excluded from the study.

As an alternative, the MultiRad 225 preclinical irradiation system, as shown in Figure 4.13, available at Maastro, was considered. Feasibility tests were performed by inserting a flexible hose into the system to simulate the OFS routing. A metal wire and a USB-C charging cable were then passed through the hose to evaluate the internal bending radius. This setup allowed for both visual and mechanical assessment of the clearance and curvature.

Figure 4.13: MultiRad 225.

It was observed that, when the hose was bent tightly—resulting in a diameter below 6 cm—the internal passage became constricted, preventing the simulated cables from passing through. This confirmed that such a bend would also impede the HS-RP200 fiber and risk permanent damage. However, these tests validated the MultiRad 225 system as a viable and safe alternative for integrating the OFS, provided that the fiber is routed with sufficient bending radius. Figure 4.14 illustrates the bending simulations performed with the hose inside the MultiRad 225 system.

Figure 4.14: Testing the bending of the OFS in the MultiRad 225.

After confirming that the OFS could be safely integrated into the MultiRad 225 system, tests could be performed to evaluate the reproducibility, linearity, accuracy, and energy dependence of the HS-RP200 within this modality. Figure 4.15 shows the experimental setup used for these measurement series.

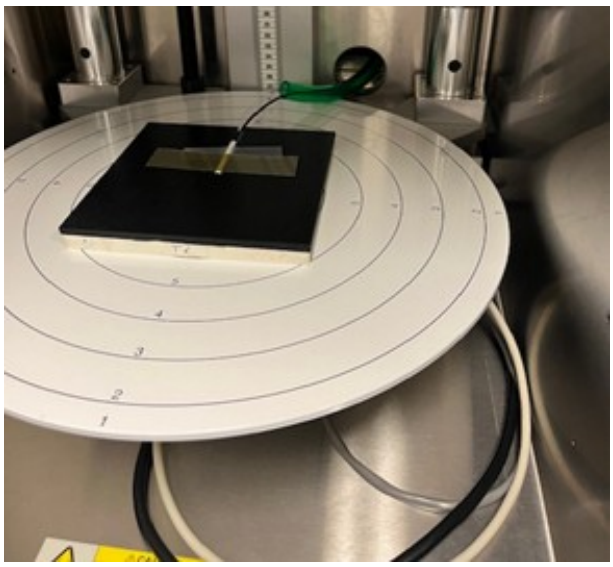

Figure 4.15: Experimental setup for tests with the MultiRad 225.

The MultiRad 225 measurements were performed using a setup consistent with the system's initial calibration settings [44]. The treatment table was lowered to its lowest possible position, corresponding to a height of 58.3 cm. This configuration minimizes the need for tight bending of the optical fiber, thereby reducing the risk of mechanical damage. The field size was set to 10×10 cm^2.

For backscatter, a 1 cm thick solid water slab was placed below the phantom. The slab containing the scintillator had a thickness of 0.5 cm. The scintillator was positioned at the center of the irradiation field, aligned with the central axis of the beam. A 0.5 mm aluminum (Al) filter was used during all irradiations to standardize beam quality.

4.4.2 Measurement Series

To assess reproducibility, ten identical measurements were conducted at an energy of 225 kVp with a prescribed dose of 1 Gy. The same procedure was repeated at 160 kVp. These two energies were selected because calibration data for the MultiRad 225 system were only available at those energy levels.

For linearity assessment, the prescribed dose was varied from 1 Gy to 8 Gy at 225 kVp. The same dose range was used for an additional set of measurements at 160 kVp.

To investigate the energy dependence of the OFS response, measurements were performed at several tube potentials between 225 kVp and 100 kVp. In each case, a dose of 4 Gy was prescribed.

To evaluate the accuracy of the OFS at the MultiRad 225, alanine dosimeters were included in multiple measurements. Radiochromic films were also placed in the setup to provide an independent comparison.

Note on Writing Assistance

During the preparation of this thesis, ChatGPT [46] (OpenAI, version 2025) was used to assist in improving the academic English formulation of certain sections. The AI tool was employed exclusively for language refinement and academic writing style improvement. In addition, ChatGPT [46] was used to assist in generating and optimizing Python scripts for data analysis. All scientific content, data analysis, and interpretation are entirely based on the author's own research and remain the sole responsibility of the author.

Chapter 5

Results

Note that all calculated and discussed uncertainties are Type A uncertainties, based solely on statistical analysis of repeated measurements. A complete uncertainty budget, incorporating both Type A and Type B components, will be developed in future research.

5.1 6 MV LINAC

Reproducibility

The results of the ten reproducibility measurements at 200 MU are presented in Table 5.1.

Table 5.1: 6 MV LINAC results at 200 MU.

Measurement	**Dose (cGy)**
1	199.91
2	199.78
3	199.79
4	199.91
5	199.94
6	199.86
7	199.94
8	199.88
9	199.96
10	199.84
Mean	**199.88**
Standard Deviation (cGy)	**0.062**
Standard Uncertainty (cGy)	**0.020**
Relative Uncertainty (%)	**0.010**

The OFS yielded a mean measured dose of 199.88 cGy across ten repeated measurements at a fixed setting of 200 MU. The standard deviation of the measurements was 0.062 cGy, calculated using the standard formula for a sample standard deviation (Equation 5.1), as described in [47]:

$$s = \sqrt{\frac{1}{n-1}\sum_{i=1}^{n}(x_i - \bar{x})^2} \tag{5.1}$$

The standard uncertainty was obtained by dividing the standard deviation by the square root of the number of measurements ($n = 10$), resulting in a value of 0.020 cGy or 0.010% relative uncertainty. Therefore, the measured dose at 200 MU can be reported as (199.88 ± 0.020) cGy.

This result demonstrates that the OFS provides highly reproducible dose measurements under fixed irradiation conditions. The very low relative uncertainty of 0.010% indicates excellent short-term stability and minimal influence of noise or system drift. This level of precision supports the use of the OFS in applications requiring consistent and repeatable dose readout.

Linearity

To assess the linearity of the OFS response, measurements were performed at multiple dose levels, starting with three repeated irradiations at 800 MU. The results are presented in Table 5.2.

Table 5.2: 6 MV LINAC results at 800 MU.

Measurement	**Dose (cGy)**
1	800.60
2	799.73
3	799.76
Mean	**800.03**
Standard Deviation (cGy)	**0.492**
Standard Uncertainty (cGy)	**0.284**
Relative Uncertainty (%)	**0.036**

The mean measured dose was 800.03 cGy. The standard deviation was 0.492 cGy, resulting in a standard uncertainty of 0.284 cGy or 0.036%.

Subsequently, three measurements were conducted at 400 MU. Table 5.3 presents the results of these measurements.

Table 5.3: 6 MV LINAC results at 400 MU.

Measurement	**Dose (cGy)**
1	399.62
2	400.56
3	400.63
Mean	**400.27**
Standard Deviation (cGy)	**0.566**
Standard Uncertainty (cGy)	**0.327**
Relative Uncertainty (%)	**0.082**

The mean measured dose was 400.27 cGy, with a standard uncertainty of 0.327 cGy or 0.082%.

Finally, a single measurement was performed at 1600 MU. Due to time constraints, only one measurement was conducted, yielding a recorded dose of 1599.31 cGy. As no standard deviation could be calculated, the associated uncertainty was estimated as the average of the other standard uncertainties to allow inclusion in the linearity analysis.

With all linearity measurements completed, Table 5.4 summarizes the different prescribed MU values alongside the corresponding OFS-measured doses and standard uncertainties.

Table 5.4: Summary of linearity measurements.

MU	**Mean dose (cGy)**	**Standard Uncertainty (cGy)**
200	199.88	0.020
400	400.27	0.327
800	800.03	0.284
1600	1599.31	0.210

For each set MU value, the mean measured dose in cGy is reported—except for 1600 MU, for which only a single measurement was available and no mean could be calculated.

The standard uncertainty associated with the 1600 MU dose was estimated by taking the mean uncertainty of the other dose levels. This approximation was necessary to enable further linearity analysis using data processing tools such as Excel and Python, employing NumPy, Matplotlib, and SciPy's curve fitting functionality.

Figure 5.1 displays the measured OFS dose as a function of the prescribed MU value. The graph demonstrates an R^2 value of 1.000, indicating excellent linearity.

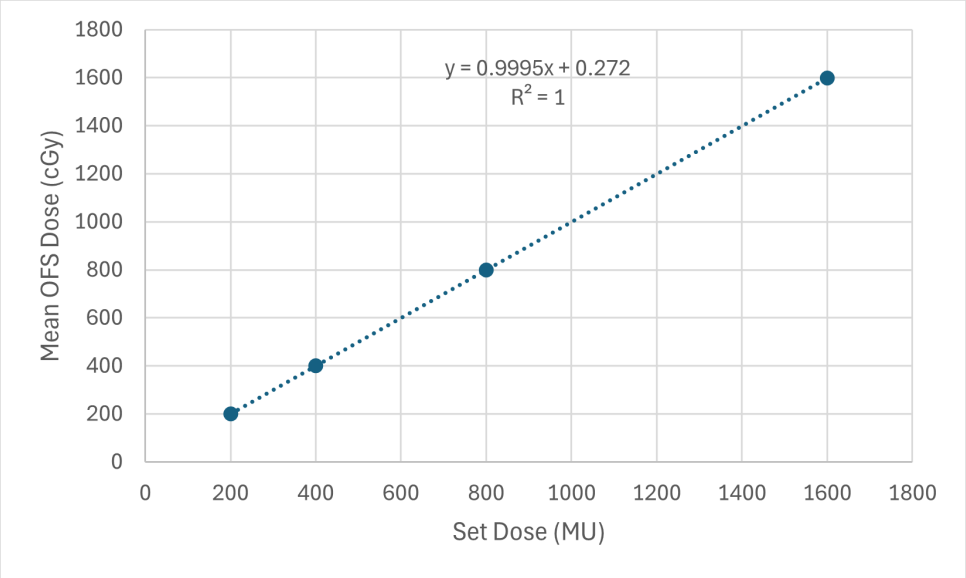

Figure 5.1: Measured dose as a function of prescribed MU (Excel).

As Excel does not support linear regression with uncertainty propagation, a weighted linear regression was performed using Python. The full script is provided in Appendix A.

Figure 5.2 presents the resulting linearity graph generated by the Python-based evaluation. For the following modalities, only the results obtained from the Python-based analysis are shown.

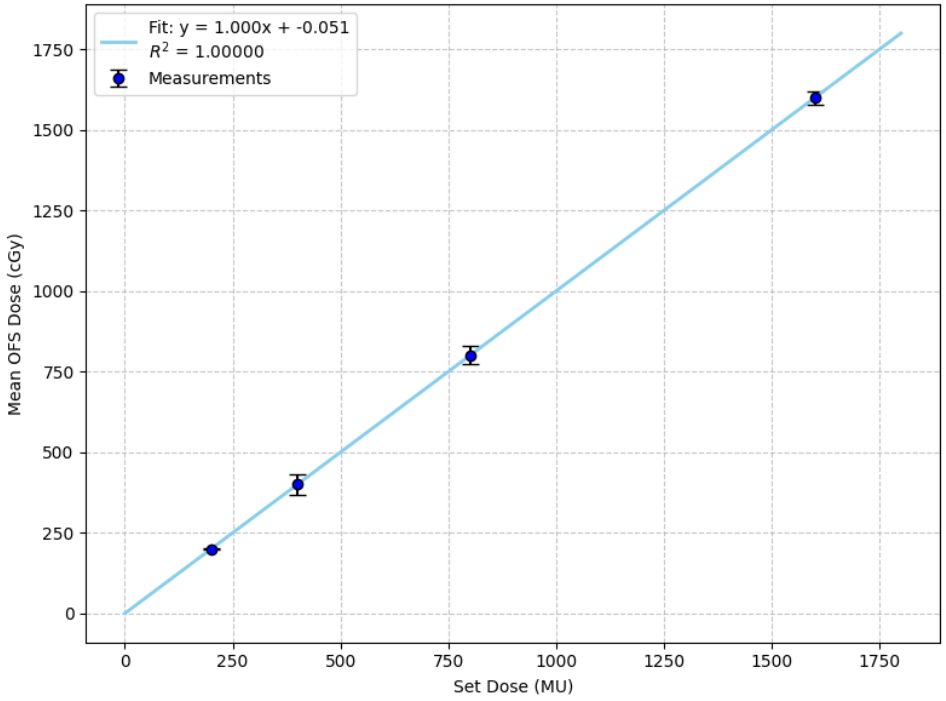

Figure 5.2: Measured dose as a function of prescribed MU (Python).

The weighted regression yielded a slope of 1.000 ± 0.000 and an intercept of (-0.051 ± 0.037)cGy, confirming the excellent linearity of the OFS response over the investigated dose range. Note that the error bars have been scaled by a factor of 100 for improved visibility; the actual uncertainties are provided in Table 5.4.

Accuracy

The third parameter investigated is the accuracy of the HS-RP200 OFS. To evaluate this, four alanine pellets were used as a reference dosimetry method across eleven measurements at 200 MU each (including the dose calibration and ten reproducibility measurements).

The expected dose delivered to the alanine pellets was 22 Gy, based on eleven irradiations of 2 Gy each. The measured dose obtained from the alanine readout was 21.77 Gy, with an associated uncertainty of 0.166 Gy, corresponding to a relative deviation of 0.76%. In comparison, the OFS reported a total dose of 21.99 Gy over the same eleven measurements, resulting in a difference of 0.99% relative to the alanine measurement. This indicates that the OFS demonstrates very good accuracy when benchmarked against alanine dosimetry.

Additional accuracy analysis was performed by including radiochromic film in the first two measurements at 800 MU. The OFS measured doses of 800.60 cGy and 799.73 cGy, whereas the corresponding film readings were 853.16 cGy and 826.65 cGy. These results correspond to deviations of 6.01% and 3.17%, respectively. Compared to alanine dosimetry, the OFS showed reduced accuracy relative to film dosimetry. A possible explanation

for this discrepancy is the use of an aged batch of radiochromic films, which may have affected measurement reliability.

A summary of the accuracy measurements is provided in Table 5.5.

Table 5.5: Summary accuracy results.

Set Dose (MU)	**OFS Dose (cGy)**	**Reference Method**	**Reference Dose (cGy)**	**Difference (%)**
2200	2198.68	Alanine	2177.20	0.99
800	800.60	Film	853.16	6.01
800	799.73	Film	826.65	3.17

5.2 Bravos afterloader

Reproducibility

The results of the ten reproducibility measurements are presented in Table 5.6, including the mean value, standard deviation, and associated uncertainty. These measurements were performed at a dwell time of 50 seconds, corresponding to a dose of 183 cGy as calculated by the TPS.

Table 5.6: Reproducibility Bravos afterloader.

Measurement	**Dose (cGy)**
1	184.94
2	182.72
3	182.53
4	182.97
5	182.59
6	181.15
7	183.09
8	182.23
9	183.00
10	182.69
Mean	**182.79**
Standard Deviation (cGy)	**0.939**
Standard Uncertainty (cGy)	**0.297**
Relative Uncertainty (%)	**0.162**

The mean measured dose was 182.79 cGy, with a standard deviation of 0.939 cGy. This results in an uncertainty of 0.297 cGy, or 0.162%. The uncertainty was calculated using Equation 5.1. Accordingly, the measured dose can be reported as (182.79 ± 0.297) cGy.

These results demonstrate the high reproducibility of the OFS when used in combination with the Bravos afterloader, with a relative uncertainty well below 1%.

Linearity

To further evaluate the linearity of the OFS response, measurements were performed at different dwell times. Specifically, five measurements were conducted at dwell times of 100 s and 40 s, and three measurements at 30 s and 10 s. Tables 5.7 - 5.10 summarize the measurement results for each dwell time, including the mean values, standard deviations, and calculated uncertainties.

Table 5.7: Linearity Bravos: 100s dwell time.

Measurement	**Dose (cGy)**
1	365.46
2	365.54
3	360.79
4	361.12
5	362.74
Mean	**363.13**
Standard Deviation (cGy)	**2.287**
Standard Uncertainty (cGy)	**1.023**
Relative Uncertainty (%)	**0.282**

At a dwell time of 100 s, the expected dose according to the TPS was 366 cGy. The OFS measured a mean dose of 363.13 cGy, with a standard deviation of 2.287 cGy, yielding an uncertainty of 1.023 cGy. The result is reported as (363.13 ± 1.023) cGy.

Table 5.8: Linearity Bravos: 40s dwell time.

Measurement	**Dose (cGy)**
1	145.99
2	145.88
3	146.57
4	144.40
5	145.95
Mean	**145.76**
Standard Deviation (cGy)	**0.806**
Standard Uncertainty (cGy)	**0.360**
Relative Uncertainty (%)	**0.247**

For a dwell time of 40 s, the expected TPS dose was 146.4 cGy. The mean OFS measurement was 145.76 cGy, with a standard deviation of 0.806 cGy and an uncertainty of 0.360 cGy. The resulting dose is reported as (145.76 ± 0.360) cGy.

Table 5.9: Linearity Bravos: 30s dwell time.

Measurement	**Dose (cGy)**
1	108.68
2	108.58
3	108.43
Mean	**108.90**
Standard Deviation (cGy)	**0.467**
Standard Uncertainty (cGy)	**0.269**
Relative Uncertainty (%)	**0.247**

At 30 s dwell time, the TPS-calculated dose was 109.8 cGy. The OFS measured an average of 108.90 cGy, with a standard deviation of 0.467 cGy and an uncertainty of 0.269 cGy. The corresponding result is (108.90 ± 0.269) cGy.

Table 5.10: Linearity Bravos: 10s dwell time.

Measurement	**Dose (cGy)**
1	36.21
2	36.43
3	36.33
Mean	**36.32**
Standard Deviation (cGy)	**0.106**
Standard Uncertainty (cGy)	**0.061**
Relative Uncertainty (%)	**0.169**

Finally, for a dwell time of 10 s (equivalent to 36.6 cGy TPS dose), the OFS measured a mean dose of 36.32 cGy with a standard deviation of 0.11 cGy. The uncertainty was calculated as 0.061 cGy, resulting in (36.32 ± 0.061) cGy.

The linearity of the OFS response was evaluated by comparing these measured values to the TPS-calculated doses. Table 5.11 provides an overview of the mean measured doses, their associated uncertainties, and the corresponding TPS doses.

Table 5.11: Linearity Bravos afterloader.

TPS Dose (cGy)	**Mean OFS Dose (cGy)**	**Uncertainty (cGy)**
36.6	36.32	0.061
109.8	108.90	0.269
146.4	145.76	0.360
183.0	182.79	0.297
366.0	363.13	1.023

Based on these data, a weighted linear regression was performed using a Python script, which is provided in Appendix B.

The resulting regression is shown in Figure 5.3.

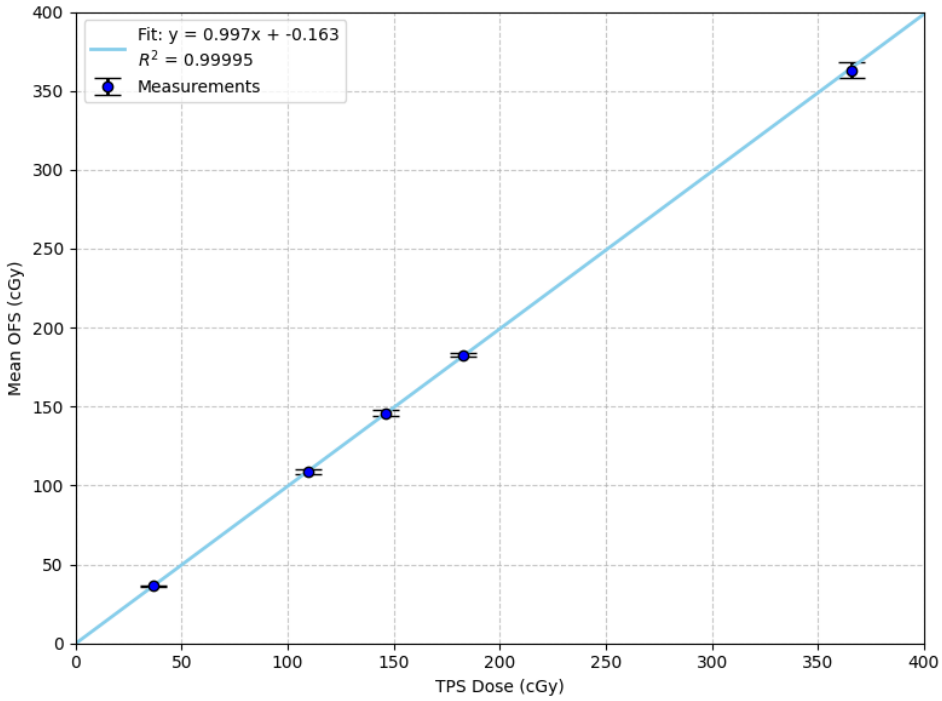

Figure 5.3: Linearity Bravos (Python).

The Python-based analysis yielded a slope of (0.997 ± 0.001) and an intercept of (-0.163 ± 0.092) cGy on the Mean OFS axis. The coefficient of determination was found to be $R^2 = 0.99995$. These results further confirm the excellent linearity of the OFS under irradiation from the Bravos afterloader. Note that the error bars have been scaled by a factor of 5 for visual clarity. Actual uncertainties are provided in Table 5.11.

Accuracy

As no alanine dosimeters or EBT3 films were included in the Bravos measurements, the accuracy could not be assessed using external reference dosimetry, as was done for the LINAC experiments. Instead, accuracy was evaluated by comparing the TPS-calculated dose values with the corresponding OFS measurements.

Table 5.12 presents the expected doses for each dwell time alongside the measured OFS values and the percentage differences.

Table 5.12: Accuracy Bravos afterloader.

TPS Dose (cGy)	**Mean OFS Dose (cGy)**	**Difference (%)**
36.6	36.32	-0.75
109.8	108.90	-0.82
146.4	145.76	-0.44
183.0	182.79	-0.12
366.0	363.13	-0.79
	Mean Difference (%)	-0.58

Across all dwell times, the difference between the TPS and OFS dose remained below 1%, with a mean deviation of −0.58%. This indicates that the OFS measurements were, on average, 0.58% lower than the TPS-calculated values.

Given the small magnitude of this deviation—well below 1%—the accuracy of the OFS measurements using the Bravos afterloader is considered excellent and within clinically acceptable limits.

5.3 Axxent Xoft

Reproducibility

The results of the ten reproducibility measurements at a scintillator depth of 0 cm are presented in Table 5.13.

Table 5.13: Corrected dose measurements with associated charge and correction factors

Measurement	**Dose (cGy)**	**Charge (pC)**	**Correction Factor**	**Corrected Dose (cGy)**
1	98.15	132.32	1.001	98.30
2	97.35	131.71	1.006	97.94
3	98.44	132.32	1.001	98.59
4	98.60	132.74	0.998	98.44
5	98.87	132.44	1.001	98.93
6	99.05	132.66	0.999	98.94
7	98.97	132.65	0.999	98.87
8	99.70	133.30	0.994	99.11
9	98.82	132.91	0.997	98.53
10	98.26	132.12	1.003	98.55
Mean		**132.52**		**98.62**
			Standard Deviation (cGy)	0.352
			Standard Uncertainty (cGy)	0.111
			Relative Uncertainty (%)	0.113

The first three columns show the measurement number, the dose measured by the OFS, and the charge measured by the ionization chamber, respectively. The fourth column lists the correction factor used to account for variations in the source depth within the applicator. This factor is based on normalization relative to the mean measured chamber charge. For example, the correction factor for the first measurement was calculated using the following formula:

$CF = \frac{132.52 \text{ pC}}{132.32 \text{ pC}} = 1.001.$

In this equation, the denominator represents the collected charge for that specific measurement, while the numerator is the average charge across all ten measurements. By multiplying the measured OFS dose by the corresponding correction factor, a corrected dose normalized for variations in source depth is obtained.

The mean corrected dose was 98.62 cGy, with a standard deviation of 0.352 cGy. This corresponds to a standard uncertainty of 0.111 cGy, or 0.113%, calculated using Formula 5.1.

Percentage Depth Dose (PDD)

This procedure was repeated for scintillator depths of 5 mm, 10 mm, and 15 mm. At each depth, three measurements were performed instead of ten. The results of these measurements are presented in Tables 5.14 to 5.16.

Table 5.14: PDD results for 5 mm depth.

Measurement	**Dose (cGy)**	**Charge (pC)**	**Correction Factor**	**Corrected Dose (cGy)**
1	67.01	132.32	0.999	66.96
2	67.54	133.19	0.993	67.06
3	66.53	131.18	1.008	67.07
Mean		**132.23**		**67.03**
			Standard Deviation (cGy)	0.058
			Standard Uncertainty (cGy)	0.034
			Relative Uncertainty (%)	0.050

At a scintillator depth of 5 mm, the mean normalized dose was 67.03 cGy, with a standard deviation of 0.058 cGy. This corresponds to a standard uncertainty of 0.034 cGy, or 0.050%.

Table 5.15: PDD results for 10 mm depth.

Measurement	**Dose (cGy)**	**Charge (pC)**	**Correction Factor**	**Corrected Dose (cGy)**
1	47.45	132.30	1.003	47.57
2	47.96	133.35	0.995	47.71
3	47.54	132.33	1.002	47.66
Mean		**132.66**		**47.65**
			Standard Deviation (cGy)	0.068
			Standard Uncertainty (cGy)	0.040
			Relative Uncertainty (%)	0.083

At a depth of 10 mm, the mean normalized dose was 47.65 cGy. The standard deviation for these measurements was 0.068 cGy, yielding a standard uncertainty of 0.040 cGy, or 0.083%.

Table 5.16: PDD results for 15 mm depth.

Measurement	**Dose (cGy)**	**Charge (pC)**	**Correction Factor**	**Corrected Dose (cGy)**
1	34.40	132.85	0.999	34.37
2	34.44	132.71	1.000	34.44
3	34.35	132.55	1.001	34.39
Mean		**132.70**		**34.40**
			Standard Deviation (cGy)	0.037
			Standard Uncertainty (cGy)	0.021
			Relative Uncertainty (%)	0.062

Finally, at a depth of 15 mm, the mean normalized dose was 34.40 cGy, with a standard deviation of 0.037 cGy and a resulting uncertainty of 0.021 cGy, or 0.062%.

With all measurements collected, the resulting PDD values were compared to the theoretical PDD curve provided in the Axxent Xoft user manual [42], shown in Figure 5.4.

Depth (mm)	10 mm cone	20 mm cone	35 mm cone	50 mm cone
0	100.0	100.0	100.0	100.0
1	88.5	86.8	89.2	89.5
2	78.2	75.5	79.6	80.4
3	69.2	66.0	71.2	72.5
4	61.2	58.1	63.8	65.9
5	54.2	51.5	57.4	60.2
6	48.1	46.1	51.8	55.4
7	42.8	41.8	47.0	51.4
8	38.3	38.3	42.8	47.9
9	34.3	35.3	39.2	44.9
10	31.0	32.9	36.0	42.2
11	28.0	30.7	33.1	39.7
12	25.5	28.5	30.5	37.3
13	23.2	26.3	28.0	34.7
14	21.0	23.7	25.5	31.9
15	19.0	20.7	23.0	28.8

Figure 5.4: Theoretical PDD of the Axxent Xoft (in %) [42].

As the measurements were performed using the 50 mm applicator cone, the final column of the theoretical table was used as the reference.

Table 5.17 summarizes the experimental PDD values alongside the corresponding theoretical values and their absolute percentage differences. The comparison reveals a mean deviation of 6.65% between the measured and theoretical PDD values.

Table 5.17: Comparison of measured and theoretical PDD values

Depth (mm)	**Mean OFS Dose (cGy)**	**Uncertainty (cGy)**	**PDD (%)**	**PDD theory (%)**	**Difference (%)**
0	98.62	0.11	100.00	100.0	0.00
5	67.03	0.034	67.966	60.2	7.77
10	47.65	0.040	48.315	42.2	6.12
15	34.40	0.021	34.877	28.8	6.08
				Mean	**6.65**

This discrepancy can be attributed to two main factors. Firstly, Figure 5.4 presents the theoretical PDD for liquid water, whereas the measurements were performed using solid water slabs, which inherently leads to differences. Secondly, the depths used in the measurements correspond only to the thicknesses of the solid water slabs. Since the HS-RP200 OFS itself has a diameter of 5 mm, an additional 2.5 mm must be added to the reported depths in Table 5.17 to account for the position of the scintillator.

By incorporating this additional depth correction, the calculations were refined. The updated results are presented in Table 5.18.

Table 5.18: Corrected PDD values after depth correction for the Axxent Xoft.

Corrected depth (mm)	**Mean OFS Dose (cGy)**	**Uncertainty (cGy)**	**PDD (%)**	**PDD theory (%)**	**Difference (%)**
2.5	98.62	0.11	76.45	76.45	0
7.5	67.03	0.034	51.96	49.65	2.31
12.5	47.65	0.040	36.94	36.00	0.94
17.5	34.40	0.021	26.66	23.73	2.93
Mean Difference (%)					**2.06**

As the corrected depths are not explicitly listed in Figure 5.4, the corresponding theoretical PDD values were obtained by interpolating between the nearest available data points. These interpolated values are also plotted in Figure 5.5. The equation of the resulting trend line was subsequently employed to estimate the theoretical PDD at a depth of 17.5 mm, as this depth fell outside the provided data range.

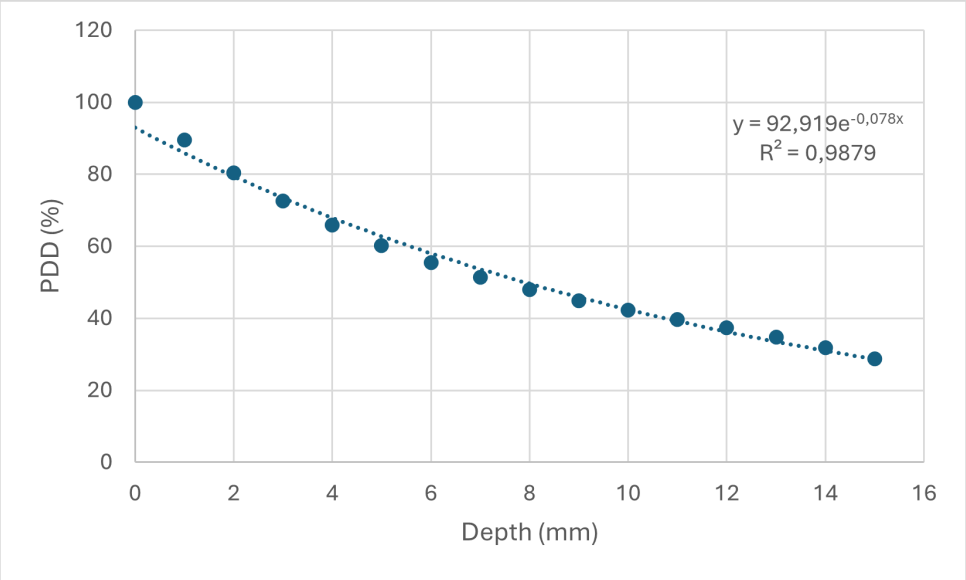

Figure 5.5: Plot of theoretical PDD Axxent Xoft.

The measured dose at a depth of 2.5 mm (corresponding to the scintillator's position) was found to be 98.62 cGy. Consequently, the dose at the surface was calculated as:

$$\frac{98.62 \text{ cGy}}{0.7645} = 129.00 \text{ cGy}.$$

The PDD values presented in the fourth column of Table 5.18 were calculated by dividing the measured OFS dose (in cGy), listed in the second column of Table 5.18, by the surface dose of 129.00 cGy.

The discrepancies between the measured PDD and the theoretical PDD were thus reduced, resulting in a mean difference of 2.06%. This remaining difference is still primarily

attributed to the variation between the liquid water medium used for the theoretical calculations and the solid water employed in the experimental setup.

The data are also presented graphically in Figure 5.6. This plot was generated using a Python script, which is provided in Appendix C.

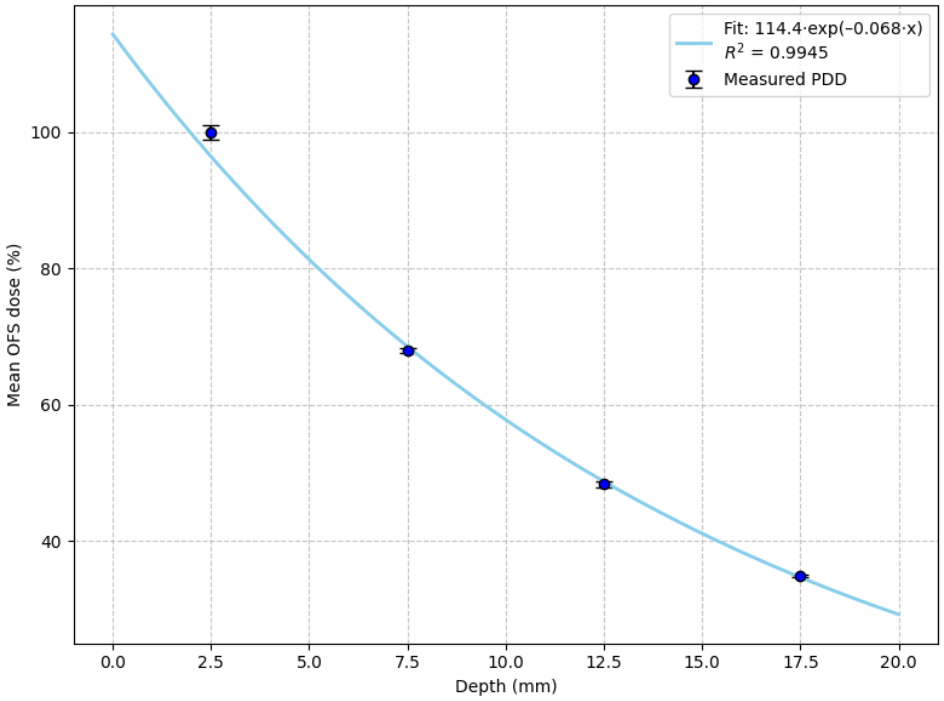

Figure 5.6: Python-analysis PDD Axxent Xoft.

This analysis yielded the equation:

$$y = 114.4 \cdot e^{-0.068x}$$

with a coefficient of determination of $R^2 = 0.9945$, demonstrating close agreement with the exponential fit. Note that the error bars have been scaled by a factor of 10 to improve visibility.

Accuracy

Finally, the accuracy of the Axxent Xoft system was evaluated. This parameter was assessed by comparing the measured dose with the expected dose, which was calculated based on the nominal dose rate and the theoretical PDD. The nominal dose rate for the Axxent Xoft, equipped with a 50 mm cone applicator, is 0.73 Gy/min. Given a dwell time of 100 seconds, the expected surface dose equals 1.22 Gy. Taking into account the scintillator depth of 2.5 mm, where the PDD is 76.45%, the expected dose at this depth is calculated as 93.01 cGy. Expected doses at other depths were similarly determined using the corresponding theoretical PDD values. A summary of these accuracy calculations is provided in Table 5.19.

Table 5.19: Accuracy evaluation for the Axxent Xoft system.

Corrected Depth (mm)	**PDD (%)**	**Expected Dose (cGy)**	**Measured OFS Dose (cGy)**	**Difference (%)**
2.5	76.45	93.01	98.62	6.03
7.5	49.65	60.41	67.03	10.96
12.5	36.00	43.80	47.65	8.79
17.5	23.73	28.87	34.40	19.13
			Mean Difference (%)	**11.23**

The mean deviation between the expected and measured doses was determined to be 11.23%. This substantial discrepancy is again primarily attributable to the difference in media: solid water used for the measurements versus liquid water assumed in the theoretical models.

Figure 5.7 presents the accuracy evaluation of the HS-RP200 for the Axxent Xoft system.

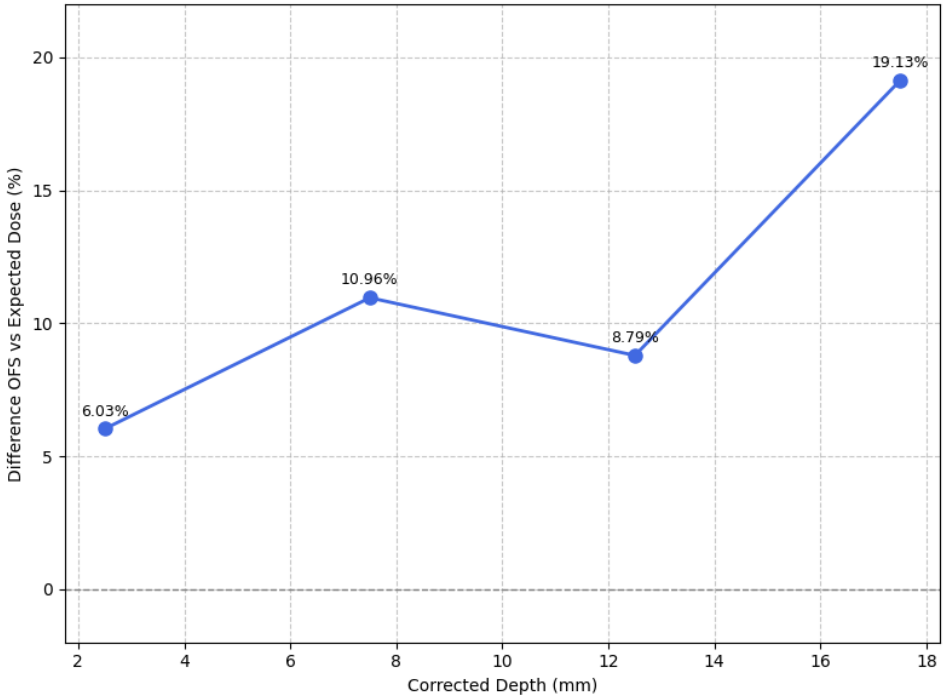

Figure 5.7: Plot of accuracy results Axxent Xoft.

The figure shows an increasing difference with increasing depth. However, it remains uncertain whether the accuracy truly decreases with depth, as the PDD value at 17.5 mm was obtained from the fitted trend line, and the experimental setup was not specifically optimized for accurate absolute dose measurements.

5.4 MultiRad225

The final modality evaluated in this study is the MultiRad 225 system. For this modality, reproducibility and linearity were assessed at 225 and 160 kVp, accuracy was evaluated

at different energies but discussed in detail only at 225 kVp, and energy dependence was investigated across photon energies ranging from 225 to 100 kVp.

Reproducibility at 225 kVp and 160 kVp

For the reproducibility measurements, a total of eleven measurements were conducted at a tube potential of 225 kVp, with a preset dose of 1 Gy. For each measurement, the system provided the exact dose that was delivered. This output allowed for correction of the measured doses, accounting for any variations in the delivered dose. The corrected results of these measurements are summarized in Table 5.20.

Table 5.20: Reproducibility measurements at 225 kVp for MultiRad 225.

Measurement	**Given dose (cGy)**	**Measured dose (cGy)**	**Correction factor**	**Corrected dose (cGy)**
1	100.5	99.49	1.0063	100.12
2	102.1	101.43	0.9906	100.47
3	100.3	99.08	1.0083	99.91
4	100.4	99.12	1.0073	99.84
5	100.2	98.93	1.0093	99.86
6	103.3	102.27	0.9791	100.13
7	100.5	100.69	1.0063	101.33
8	100.4	100.69	1.0073	101.43
9	102.0	101.48	0.9915	100.62
10	100.4	100.22	1.0073	100.96
11	102.4	102.30	0.9877	101.04

The first column of Table 5.20 lists the measurement number, while the second column presents the exact dose delivered, as reported by the MultiRad 225 system. The third column contains the dose measured by the HS-RP200. The fourth column displays the correction factor, which is calculated by dividing the mean of all delivered doses by the exact dose delivered for each individual measurement. Multiplying the measured dose by this correction factor yields the corrected dose, provided in the final column.

The final mean value for the corrected dose was determined to be 100.52 cGy. For these eleven measurements, the standard deviation, absolute uncertainty, and relative uncertainty were calculated. The results of these statistical analyses are summarized in Table 5.21.

Table 5.21: Uncertainty results at 225 kVp.

Parameter	**Value**
Standard deviation (cGy)	0.596
Standard Uncertainty (cGy)	0.180
Relative Uncertainty (%)	0.179

This procedure was repeated at a tube potential of 160 kVp. These two tube potentials

were selected as they correspond to the calibration settings of the system. At 160 kVp, a total of ten measurements were conducted, each with a preset dose of 1 Gy. The results of these measurements are presented in Table 5.22.

Table 5.22: Reproducibility measurements at 160 kVp for MultiRad 225.

Measurement	**Given dose (cGy)**	**Measured dose (cGy)**	**Correction factor**	**Corrected dose (cGy)**
1	102.1	102.93	0.9992	102.85
2	101.9	101.69	1.0012	101.81
3	102.0	101.92	1.0002	101.94
4	102.1	101.76	0.9992	101.68
5	101.4	101.35	1.0061	101.97
6	102.1	102.93	0.9992	102.85
7	102.2	103.23	0.9982	103.05
8	102.2	103.51	0.9982	103.33
9	102.1	101.95	0.9992	101.87
10	102.1	103.08	0.9992	103.00

The correction procedure was performed in the same manner as for the 225 kVp measurements. The mean corrected dose at 160 kVp was determined to be 102.44 cGy. The standard deviation, along with the absolute and relative uncertainties corresponding to these results, are presented in Table 5.23.

Table 5.23: Uncertainty results at 160 kVp.

Parameter	**Value**
Standard deviation (cGy)	0.629
Standard Uncertainty (cGy)	0.199
Relative Uncertainty (%)	0.194

The calculated uncertainties are 0.179% at 225 kVp and 0.19% at 160 kVp, resulting in an overall uncertainty of 0.19%. These results demonstrate that the HS-RP200 operates as a highly reproducible detector for this modality.

Linearity at 225 kVp and 160 kVp

To evaluate the linearity of the HS-RP200 with this modality, additional measurements were conducted at varying preset doses. Following the reproducibility measurements performed at a dose of 1 Gy, three measurements were carried out at preset doses of 2, 4, 6, and 8 Gy, all at a tube potential of 225 kVp. The results of these measurements are summarized in Table 5.24.

Table 5.24: Linearity measurements at 225 kVp for MultiRad 225.

Set Dose (cGy)	**Measured OFS Dose (cGy)**	**Standard Deviation (cGy)**	**Standard Uncertainty (cGy)**	**Relative Uncertainty (%)**
100	100.52	0.596	0.180	0.179
200	203.24	0.774	0.447	0.220
400	405.41	0.860	0.497	0.123
600	608.12	1.356	0.78 3	0.129
800	810.12	2.142	1.237	0.153

The first column of Table 5.24 lists the prescribed dose, while the second column presents the mean dose measured by the HS-RP200. The final three columns provide the standard deviation, as well as the absolute and relative uncertainties, calculated from the three measurements performed at each prescribed dose. All relative uncertainties fall within the range of 0.12% to 0.22%, with an average relative uncertainty of 0.161%.

Based on these data, the mean dose measured by the OFS is plotted as a function of the prescribed dose. This relationship is presented in Figure 5.8. The plot was generated using a Python script, which is provided in Appendix D.

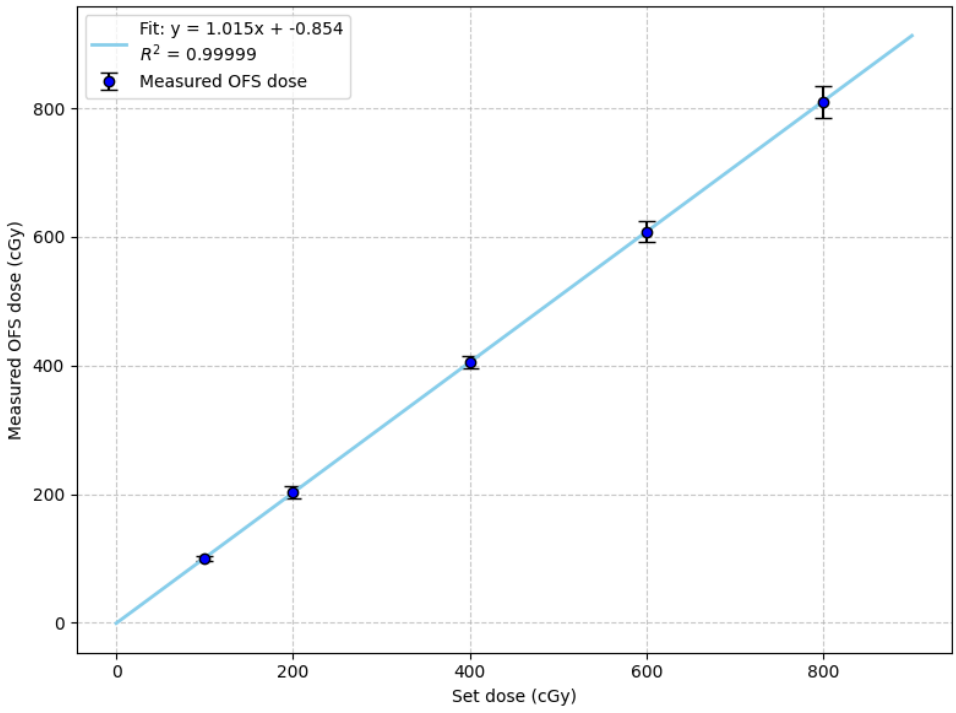

Figure 5.8: Linearity at 225 kVp for MultiRad 225 (Python).

This analysis demonstrates excellent linearity, with a coefficient of determination of $R^2 \approx 1$. The resulting trend line can be described by:

$$\text{Measured OFS Dose} = 1.015 \times \text{Set Dose} - 0.854.$$

These results confirm the excellent linearity of the HS-RP200 for the MultiRad 225 at 225 kVp. Note that the error bars have been scaled by a factor of 20 to improve visibility.

The linearity measurements were subsequently repeated at a tube potential of 160 kVp. At this setting, three additional measurements were performed at preset doses of 2 Gy and 4 Gy, and two measurements at 8 Gy. The results are presented in Table 5.25, following the same structure as the linearity measurements at 225 kVp.

Table 5.25: Linearity measurements at 160 kVp.

Set Dose (cGy)	**Measured OFS Dose (cGy)**	**Standard Deviation (cGy)**	**Standard Uncertainty (cGy)**	**Relative Uncertainty (%)**
100	102.44	0.629	0.199	0.194
200	202.66	0.393	0.227	0.112
400	402.66	2.233	1.289	0.320
800	803.47	5.933	4.196	0.522

In this case, all relative uncertainties range between 0.11% and 0.53%, with an average relative uncertainty of 0.287%. A Python-based weighted analysis was also performed for these data, and the results are presented in Figure 5.9. The corresponding Python script is provided in Appendix E.

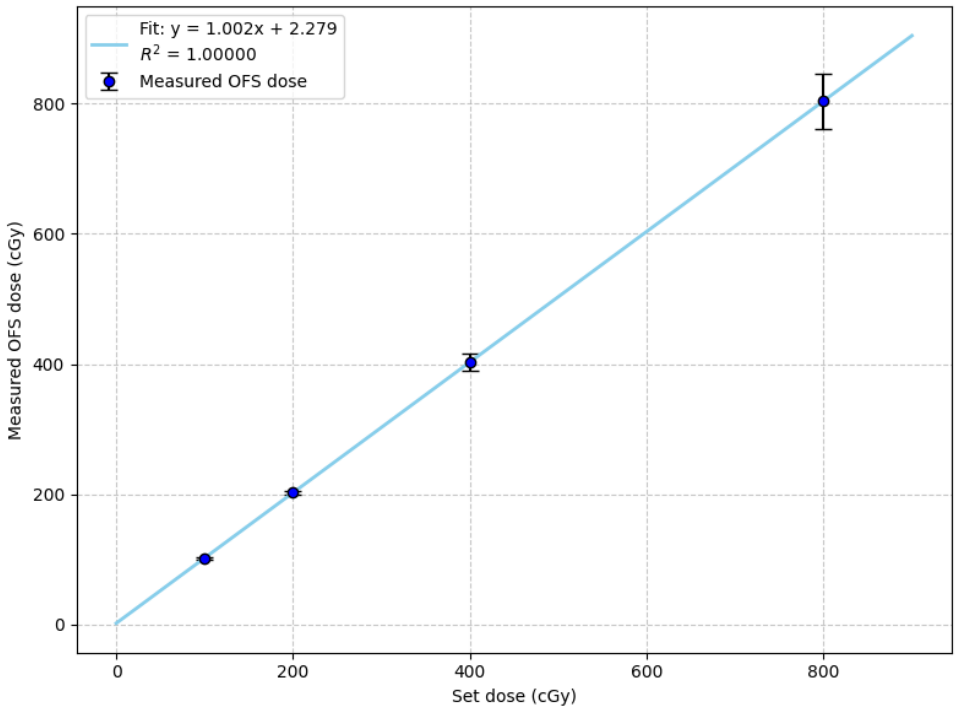

Figure 5.9: Linearity at 160 kVp for MultiRad 225 (Python).

This analysis yielded a coefficient of determination of $R^2 = 1$, with the equation of the linear trend line given by:

$$\text{Measured OFS Dose} = 1.002 \times \text{Set Dose} + 2.279.$$

The slope obtained from this analysis was 1.002 ± 0.0024, while the intercept on the measured OFS dose axis was determined to be 2.279 ± 0.385 cGy. These results confirm the excellent linearity of the OFS response, as indicated by the perfect R^2 value, and demonstrate excellent agreement between the data and the fitted model. Note that the error bars in the figure have been scaled by a factor of 10 to improve visibility.

Accuracy

To assess the accuracy of the HS-RP200 for this modality, alanine pellets and radiochromic films were incorporated into the experimental setup as reference dosimetry methods. A total of ten alanine pellets were used across multiple measurements. The first pellet was irradiated during several measurements, including the final reproducibility measurement at 1 Gy, four measurements at 2 Gy, and two measurements at 4 Gy, resulting in a cumulative dose of 17 Gy. The remaining pellets were each used for a single measurement. Table 5.26 summarizes the dose received by each pellet, along with the corresponding tube potential at which irradiation was performed.

Table 5.26: Irradiation doses for alanine pellets at various tube potentials.

Alanine Number	**Planned Dose (cGy)**	**Tube Potential (kVp)**
1	1716.0	225
2	403.4	225
3	602.1	225
4	801.9	225
5	400.0	160
6	800.9	160
7	400.2	200
8	401.8	180
9	401.5	140
10	400.3	100

The doses listed in Table 5.26 correspond to the exact doses delivered, as reported by the MultiRad 225 system. Following the readout of the alanine pellets, the doses measured by the HS-RP200 were compared to the alanine measurements, serving as a reference. A summary of these results is presented in Tables 5.27 and 5.28.

Table 5.27: Measured doses for alanine and OFS.

Planned Dose (cGy)	**Tube Potential (kVp)**	**Alanine Dose (cGy)**	**Alanine Unc. (cGy)**	**OFS Dose (cGy)**	**OFS Unc. (cGy)**
1716.0	225	1773.18	13.295	1721.86	3.211
403.4	225	413.98	5.748	406.13	0.757
602.1	225	627.95	6.619	609.05	1.136
801.9	225	831.60	7.627	812.46	1.515
400.0	160	391.75	5.672	405.23	0.756
800.9	160	793.03	7.429	799.28	1.490
400.2	200	418.67	5.765	404.19	0.754
401.8	180	406.94	5.723	403.44	0.752
401.5	140	393.15	5.677	402.00	0.750
400.3	100	373.43	5.612	389.08	0.726

Table 5.28: Accuracy evaluation based on difference and combined uncertainty.

Planned Dose (cGy)	**Tube Potential (kVp)**	**Difference (%)**	**Combined Unc. (%)**
1716.0	225	-2.89	0.77
403.4	225	-1.90	1.40
602.1	225	-3.01	1.07
801.9	225	-2.30	0.94
400.0	160	3.44	1.46
800.9	160	0.79	0.96
400.2	200	-3.46	1.39
401.8	180	-0.86	1.42
401.5	140	2.25	1.46
400.3	100	4.19	1.52

The first two columns of Table 5.27 present the planned dose in cGy as given by the MultiRad 225 preclinical X-ray cabinet, and the tube potential at which the measurements were performed. The third column lists the dose measured by each individual alanine pellet, without applying any correction factor for the tube potential, while the corresponding absolute uncertainties are reported in the fourth column. The fifth and sixth columns contain the OFS-measured doses and their respective uncertainties.

The third column of Table 5.28 shows the relative difference between the OFS measurements and the reference doses obtained from the alanine pellets. The final column lists the combined relative uncertainties. These combined uncertainties are calculated by dividing the absolute uncertainties by the reference dose and multiplying by 100%. The absolute uncertainty is determined as the square root of the sum of the squared individual uncertainties (quadrature sum).

The uncertainty on the OFS measurements was estimated by multiplying the total measured dose by the average relative uncertainty obtained from the reproducibility measurements at 225 kVp and 160 kVp.

The mean relative difference between the OFS dose and the reference dose was found to be -0.375%, with a standard deviation of 2.84% for the relative differences. The mean combined relative uncertainty was calculated to be 1.24%.

The second reference method employed was EBT3 film dosimetry. For this method, a film was included in one of the three linearity measurements at each dose level. In this way, six films with increasing dose levels were obtained: 0, 1, 2, 4, 6, and 8 Gy. These six films were used to establish the calibration curve in the FilmQA Pro software, which was subsequently used to analyze the films. The remaining films were utilized in the measurements to assess the energy dependence of the detector, as described in the following section. These measurements were conducted at tube potentials of 200, 180, 140, and 100 kVp, respectively. For each measurement, the prescribed dose was 4 Gy. A summary of the results is provided in Table 5.29.

Table 5.29: Comparison between EBT3 film and OFS measurements for accuracy evaluation.

Film Dose (cGy)	**Film Unc. (cGy)**	**OFS Dose (cGy)**	**OFS Unc. (cGy)**	**Difference (%)**	**Combined Unc. (%)**
400.3	15.2	404.19	0.746	0.972	3.802
413.2	15.7	403.44	0.746	-2.363	3.804
411.1	16.3	402.00	0.746	-2.213	3.969
416.4	16.2	389.08	0.746	-6.560	3.895

The first two columns present the doses measured by the films and by the scintillator, respectively. The third and fourth columns provide the absolute and relative differences between the two dose measurements. The final two columns report the combined absolute uncertainty and the combined relative uncertainty. The mean relative difference between the film doses and the OFS doses was found to be -2.54%, with a standard deviation of 3.09% for the relative differences. The mean of the combined relative uncertainties was 3.87%.

The comparison with the EBT3 films was also performed using the one-scan calibration method. In this approach, two reference films irradiated with doses of 0 Gy and 8 Gy were included in the same scan alongside the four films under investigation. Based on this calibration, the mean relative difference was found to be -3.09%, with a standard deviation of 2.97%. The mean combined relative uncertainty was 3.83%. Although this method is slightly less accurate than the full calibration series, the results are very similar. This is expected, as the calibration films were irradiated simultaneously with the films being analyzed.

The comparison between OFS and alanine dosimetry yielded a mean deviation of –0.38% with a combined relative uncertainty of 1.24%. For the film measurements, a mean devi-

ation of –2.54% with a combined relative uncertainty of 3.87% was observed. The slightly larger deviation observed in the film comparison may partly be attributed to the energy dependence of the OFS, as these measurements were performed at 100 kVp. This aspect will be further investigated in the following section. In both cases, the deviations lie within the combined uncertainties, indicating no statistically significant systematic difference between the OFS and the reference dosimetry methods. This confirms that the OFS provides accurate dose measurements within experimental uncertainty limits.

As the differences between the planned dose and the doses measured by the reference methods (alanine and EBT3 films) increase at lower energies, only the measurements at 225 kVp are included in the discussion of the HS-RP200 accuracy for this modality. These discrepancies are primarily attributed to the absence of an implemented correction factor for alanine dosimetry. Additionally, there may be uncertainties associated with the planned dose as reported by the MultiRad 225 system. A comprehensive assessment of the HS-RP200 accuracy, including type B uncertainties, will be conducted in future research.

Energy Dependence

The energy dependence of the HS-RP200 OFS was evaluated by comparing the measured dose at different tube potentials to the exact dose delivered by the MultiRad 225 system. The results are summarized in Table 5.30.

Table 5.30: Energy dependence of the OFS response for the MultiRad 225 system.

Energy (kVp)	**Given Dose (cGy)**	**Measured Dose (cGy)**	**Difference (%)**
225	401.7	405.41	1.35
200	400.2	403.43	0.86
180	401.8	404.29	1.07
160	400.9	402.65	0.66
140	401.5	402.56	0.64
100	400.3	388.45	2.89

The relative differences range from 0.64% to 2.89%, with the largest deviation observed at 100 kVp, which indicates a minor energy dependence at lower photon energies.

Although measurements were performed at multiple tube potentials down to 100 kVp, no measurements were conducted at lower energies due to time constraints during the experimental period. However, additional measurements at lower photon energies could be performed in future studies to further investigate the energy dependence of the HS-RP200 at very low energies, where more pronounced variations in response might be expected due to changes in photon interaction processes.

Chapter 6

Discussion

The primary aim of this study was to systematically evaluate the performance of the HS-RP200 OFS under a wide range of irradiation conditions representative of both clinical and preclinical radiotherapy. The investigation included four different modalities: a clinical Varian Truebeam LINAC (6 MV), HDR brachytherapy with the Varian Bravos afterloader, electronic brachytherapy using the Axxent Xoft system, and preclinical X-ray irradiation using the Precision MultiRad 225 system. For each modality, reproducibility, linearity, and accuracy were assessed, while energy dependence was also studied using the MultiRad 225 system.

6.1 Reproducibility

Across all used modalities, the HS-RP200 demonstrated excellent short-term reproducibility. For the 6 MV LINAC, a relative uncertainty of 0.0098% was observed, representing essentially negligible variation between repeated measurements. The standard deviation of 0.03% is comparable to the value reported by *Beddar et al.* [6], who observed a variation of approximately 0.05% for 6 MV photon beams using the Varian Clinic 2100C linear accelerator. The very low uncertainty confirms the excellent stability of the OFS system in conventional MV photon beams, where the detector's water equivalence and minimal energy dependence are expected to contribute to consistent signal output.

Comparable reproducibility was found for the HDR brachytherapy modality, with a relative uncertainty of 0.162%. Although slightly higher than for the LINAC, this difference may be explained by inherent variations in source positioning, dwell time control, or small mechanical fluctuations in the Bravos afterloader system. Nevertheless, reproducibility remained well below the 1% target commonly used as a clinical acceptance threshold [48].

For the Axxent Xoft electronic brachytherapy system, reproducibility remained within 0.113% after correction for small variations in source positioning using ionization chamber readings. Without these corrections, slightly larger fluctuations were observed, underscoring the importance of geometric precision in low-energy X-ray setups.

The MultiRad 225 system exhibited relative uncertainties below 0.2% at both 225 kVp and 160 kVp. While these values are still excellent, they are marginally higher compared

to the LINAC results. This may reflect increased sensitivity of the OFS response to energy fluctuations at lower photon energies, where photoelectric interactions contribute more significantly to signal generation. Additionally, minor uncertainties in source output stability and positioning accuracy in preclinical systems may have contributed.

Table 6.1 provides a comparison of the reproducibility results of the HS-RP200 across all used modalities.

Table 6.1: Comparison of reproducibility results across modalities.

	LINAC	**Bravos**	**Xoft**	**MultiRad 225 (225 kVp)**	**MultiRad 225 (160 kVp)**
Mean Dose (cGy)	199.880	182.790	98.620	100.518	102.436
Standard Deviation (cGy)	0.062	0.939	0.352	0.596	0.629
Relative Std. Dev. (%)	0.031	0.514	0.357	0.593	0.614
Standard Uncertainty (cGy)	0.020	0.297	0.111	0.180	0.199
Relative Uncertainty (%)	0.0098	0.162	0.113	0.179	0.194

Table 6.1 shows that the relative standard deviation remains below 1% for all investigated modalities. The highest relative standard deviation was observed for the MultiRad 225 at 160 kVp, where it reached 0.614%. The corresponding relative uncertainty, representing the type A standard uncertainty, is therefore consistently below 1% across all modalities. The values range from 0.01% for the LINAC to 0.19% for the MultiRad 225 at 160 kVp. Since all relative uncertainties remain below 0.2%, these results demonstrate excellent reproducibility of the HS-RP200 system.

Moreover, the reproducibility satisfies the requirements specified by the IAEA [48] (TRS-398), which recommend tolerances of 1% for high-energy photons and 2.3% and 1.8% for low- and medium-energy kilovoltage X-rays, respectively. It should be noted, however, that these values represent only the type A standard uncertainty and do not account for additional sources of uncertainty (type B uncertainties), such as TPS uncertainties, equipment-related uncertainties, or positioning variations, which contribute to the overall combined uncertainty.

The consistently low relative uncertainties observed across all modalities confirm the excellent stability and repeatability of the HS-RP200 system under a wide variety of irradiation conditions. The slightly higher uncertainties observed for the MultiRad 225 system, particularly at 160 kVp, may be attributed to the increased influence of photoelectric interactions and greater sensitivity to positioning inaccuracies at lower photon energies. Nevertheless, the reproducibility consistently remained well below clinically acceptable thresholds across all energy ranges, supporting the feasibility of implementing the HS-RP200 for routine clinical quality assurance and dosimetric audits in both external beam radiotherapy and brachytherapy settings.

6.2 Linearity

The HS-RP200 demonstrated excellent linearity across all investigated modalities. Weighted linear regression analysis using Python confirmed that the slopes remained within 1% of unity for all modalities, with coefficients of determination (R^2) consistently exceeding 0.999, indicating an excellent agreement between measured and prescribed doses.

For the 6 MV LINAC, the slope was 1.000 ± 0.000, reflecting nearly perfect proportionality between measured dose and monitor units across the entire tested dose range, up to 1600 MU. This performance is consistent with previous studies on scintillator dosimetry, which reported no significant deviations from linearity for MV photon beams [6].

For the HDR brachytherapy modality (Bravos afterloader), a slope of 0.997 ± 0.001 was obtained, remaining well within 1% of unity. The slight negative deviation may be attributed to small uncertainties related to dwell time control or positioning accuracy in the Bravos system. Importantly, linearity was preserved even at the highest tested dwell times, up to 366 cGy.

For the MultiRad 225 preclinical system, excellent linearity was observed at both 225 kVp and 160 kVp tube potentials, with regression slopes of 1.015 ± 0.001 and 1.002 ± 0.0024, respectively. The slight over-response observed at 225 kVp may be explained by small energy-dependent variations in scintillation light output at lower photon energies, where photoelectric absorption plays a more significant role. Table 6.2 and 6.3 provides a comparison of the linearity performance of the HS-RP200 across all investigated modalities.

Table 6.2: Comparison of linearity results across modalities.

Modality	**Dose Range**	**Slope** m	Δm	**Intercept**	**Δ Int.**	R^2
LINAC	200 - 1600 MU	1.000	0.000	-0.051	0.037	1
Bravos	36.6 - 366 cGy	0.997	0.001	-0.163	0.092	1
MultiRad 225 (225 kVp)	100 - 800 cGy	1.015	0.001	-0.854	0.235	0.999
MultiRad 225 (160 kVp)	100 - 800 cGy	1.002	0.002	2.279	0.385	1

Table 6.3: Deviations from perfect linearity for all investigated modalities.

Modality	**Slope** (m)	**Deviation (%)**	**Uncertainty (%)**
LINAC	1.000	0.0	0.0
Bravos	0.997	0.3	0.1
MultiRad 225 (225 kVp)	1.015	1.5	0.1
MultiRad 225 (160 kVp)	1.002	0.2	0.2

The deviations from linearity, presented in Table 6.3, were calculated by determining the absolute difference between the measured slope and the ideal slope of 1.00, and multiplying this value by 100%. The associated uncertainties were obtained by multiplying the uncertainty of the slope by 100%.

The observed deviations from perfect linearity ranged from 0% for the LINAC to 1.5% for the MultiRad 225 at 225 kVp. These findings confirm the excellent linearity performance of the HS-RP200 across all investigated modalities. The R^2 values consistently reached 1.000 (or 0.999), indicating excellent agreement between the linear regression models and the measured data.

Figure 6.1 presents a comparison of the HS-RP200 linearity deviations observed across the different irradiation modalities.

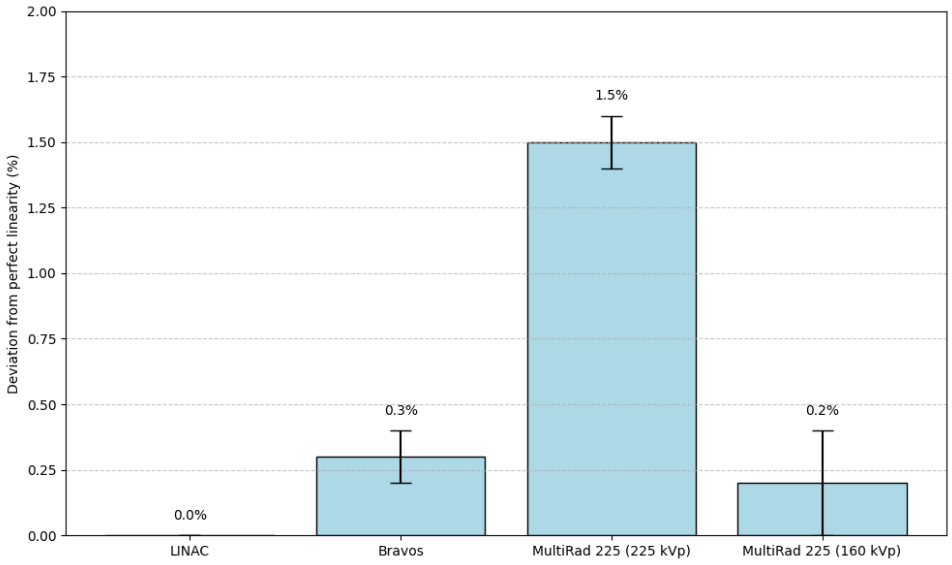

Figure 6.1: Linearity results comparison.

At present, no formal international standard specifies maximum allowable linearity deviations for independent external dosimetry systems. However, based on empirical evidence from previous scintillator studies [6] and prevailing clinical QA practices, linearity deviations within 1% are generally considered acceptable for high-precision dosimetric applications.

Overall, the HS-RP200 demonstrated excellent linearity throughout the entire dynamic range of investigated doses and energies, even when different calibration protocols (i.e., five-component correction for LINAC and Bravos, versus fluorescence-scintillation correction for Xoft and MultiRad) were applied. These results confirm the suitability of the HS-RP200 for accurate dose quantification across both high- and low-energy photon fields, with strong potential for clinical quality assurance, patient-specific verification, and dosimetric audits.

6.3 Percentage Depth Dose

For the Axxent Xoft system, PDD measurements were assessed instead of conventional linearity analysis, as PDD provides a practical surrogate to evaluate the consistency of dose response as a function of depth in electronic brachytherapy applications. The observed PDD showed a 6.65% deviation from the theoretical values. After correcting for

the actual position of the sensitive scintillating volume within the detector tip, this deviation was reduced to 2.06%. The remaining difference can likely be attributed to the use of solid water slabs in the experimental setup, whereas the theoretical reference data are based on liquid water measurements. Such differences between solid and liquid water can introduce small but systematic discrepancies in depth dose comparisons. Additionally, minor uncertainties related to detector positioning and source alignment may have contributed to the residual deviation.

6.4 Accuracy

The accuracy of the HS-RP200 was evaluated across all modalities using reference dosimetry systems, including alanine pellets, EBT3 films, and TPS data where no physical references were available.

For the LINAC measurements, the HS-RP200 showed excellent agreement with alanine dosimetry, with a relative difference of 0.987%. These results are consistent with previous studies validating plastic scintillator accuracy for MV photon beams [6]. The film dosimetry measurements, however, exhibited larger deviations of up to 6.01%. This discrepancy can likely be attributed to film aging effects, as the batch of EBT3 films had been stored for an extended period prior to use, potentially affecting their calibration response [36]. Despite these larger differences for film, the alanine results confirm the high accuracy of the HS-RP200 under LINAC irradiation.

For the Bravos afterloader, no external reference dosimetry was available during the study. Accuracy was therefore assessed by comparing the OFS measurements directly to the dose values calculated by the TPS. Across all tested dwell times, mean deviations remained well below 1%, indicating excellent agreement between the OFS and the planned dose delivery for HDR brachytherapy.

For the Axxent Xoft electronic brachytherapy system, the accuracy was evaluated by comparing the expected dose with the measured OFS dose at different depths. After correcting for the position of the sensitive volume inside the HS-RP200 detector, the mean difference was 11.23%. This remaining deviation can likely be attributed to the use of solid water slabs in this study, as opposed to liquid water phantoms used to derive the theoretical reference values. Nevertheless, it should be noted that the experimental setup employed here was not specifically optimized for a full accuracy assessment of the scintillator. However, a preliminary evaluation of the accuracy was still performed based on the available data.

For the MultiRad 225 system, excellent agreement was observed between OFS measurements and alanine dosimetry. A total of ten measurements were performed using alanine pellets. However, only those obtained at a tube potential of 225 kVp were considered for accuracy evaluation. The mean difference between the alanine reference doses and the OFS measurements was 2.53%, with a combined uncertainty of 1.04%, confirming the high accuracy of the HS-RP200 for dosimetry in preclinical X-ray cabinet systems. This difference is slightly larger than that observed for the LINAC measurements, which can be partly attributed to the difference in photon energy (225 kVp compared to 6 MV),

leading to increased energy dependence effects at lower photon energies.

The combined uncertainties were calculated by taking the square root of the sum of the squared individual uncertainties associated with both the OFS and the reference dosimetry systems. For the Bravos afterloader and Axxent Xoft modalities, where no external reference dosimetry was available for accuracy assessment, no combined uncertainty could be determined.

Table 6.4 and Figure 6.2 summarize the accuracy results across all used modalities. When the combined uncertainty was not available, no error bars are displayed in Figure 6.2.

Table 6.4: Comparison of accuracy results across all modalities.

Modality	**Reference Method**	**OFS - Reference Difference (%)**	**Combined Uncertainty (%)**
LINAC	Alanine	0.987	0.763
LINAC	EBT3 Film	4.594	5.419
Bravos	TPS	0.583	/
Xoft	Calculated Dose	11.23	/
MultiRad 225	Alanine	2.53	1.04

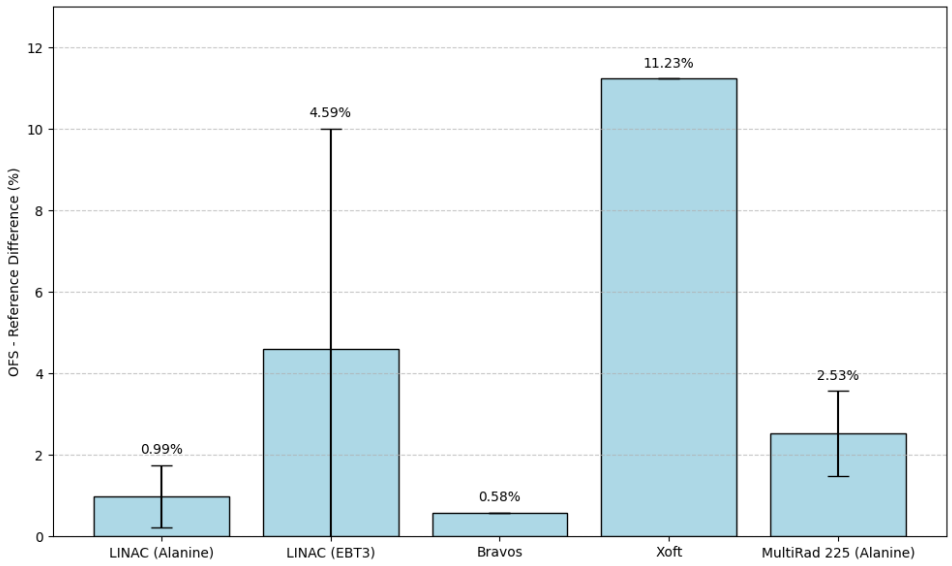

Figure 6.2: Accuracy results comparison.

Overall, the HS-RP200 demonstrated consistent accuracy across a broad range of irradiation modalities, with relative deviations from reference systems generally remaining well within clinically acceptable limits for independent dosimetric verification.

6.5 Energy Dependence

Energy dependence was systematically evaluated for the MultiRad 225 system. Across photon energies ranging from 225 kVp down to 100 kVp, relative differences between

the measured OFS doses and the prescribed doses ranged from 0.64% to 2.89%. The prescribed doses were directly determined from the MultiRad 225 system output. The system reported the exact delivered dose following each irradiation.

The largest deviation was observed at 100 kVp, which may reflect enhanced photon interaction effects at lower energies (e.g., increased photoelectric absorption sensitivity in the scintillator material) [5]. The fact that the MultiRad 225 was calibrated only at 225 and 160 kVp, and not at 100 kVp, could also contribute to additional uncertainties. While the observed deviations are small, they indicate a minor but non-negligible energy dependence at lower photon energies. Nevertheless, these deviations remain within clinically acceptable tolerances for preclinical kV X-ray dosimetry and are consistent with typical uncertainties reported for low-energy photon dosimetry systems [49].

No measurements were conducted at photon energies below 100 kVp due to time constraints. Future studies could further extend these measurements to fully characterize the energy response of the HS-RP200 system at very low photon energies and to establish a correction factor applicable for low-energy dosimetry.

6.6 Reflection on Objectives

Overall, the results presented in this study address the sub-objectives outlined in Section 1.3. The reproducibility, linearity, and accuracy of the HS-RP200 were successfully evaluated across four irradiation modalities, with PDD measurements used for the Axxent Xoft system. Energy dependence was also investigated using the MultiRad 225 preclinical X-ray cabinet. In addition, preliminary estimations of type A uncertainties were performed for all investigated parameters. These findings provide a comprehensive first assessment of the HS-RP200 system under a broad range of clinically and preclinically relevant irradiation conditions.

6.7 Limitations and Future Work

Several limitations of this study should be noted. First, while short-term reproducibility was excellent, long-term stability and potential degradation effects of the HS-RP200 were not assessed and would require extended monitoring over months or years of clinical use. Second, although extensive calibration procedures were implemented, additional sources of uncertainty may still contribute to the total measurement uncertainty, including temperature variations, uncertainties related to the irradiation modalities themselves, and minor misalignments during the experimental setup.

For the Axxent Xoft modality, the assessment of accuracy was limited to a preliminary evaluation based on theoretical PDD calculations, rather than direct reference dosimetry measurements. Furthermore, the limited number of energy points included in the energy dependence study leaves room for refinement, particularly below 100 kVp, where stronger deviations may arise. Future research could also investigate additional brachytherapy applicator geometries and systematically assess the OFS response under strong fiber bending conditions, where signal loss or spectral distortion may occur.

Lastly, while the uncertainties discussed in this study are all Type A uncertainties, a complete uncertainty budget will be developed in future research.

6.8 Overall Clinical Implications

The HS-RP200 optical fiber scintillator demonstrates excellent reproducibility, linearity, and accuracy across a wide range of irradiation modalities, photon energies, and clinical contexts, including both MV and kV applications. Its water-equivalence, real-time readout capability, and very small active volume provide significant advantages for in vivo dosimetry and preclinical setups where conventional detectors are less suitable. Importantly, the detector performed consistently well for both external beam radiotherapy and brachytherapy, supporting its versatility for implementation in patient-specific quality assurance programs, treatment commissioning protocols, and independent dosimetric audits.

Chapter 7

Conclusion

In this study, the dosimetric performance of the HS-RP200 optical fiber scintillator was comprehensively evaluated under a wide range of irradiation modalities, encompassing both clinical and preclinical applications. The investigated modalities included a Varian Truebeam linear accelerator (6 MV), HDR brachytherapy using the Varian Bravos afterloader, electronic brachytherapy with the Axxent Xoft system, and preclinical X-ray irradiation with the Precision MultiRad 225 system.

The HS-RP200 demonstrated excellent reproducibility across all modalities, with relative uncertainties (type A) consistently remaining below 0.2%. Linearity analyses, performed using Python-based weighted regression methods, confirmed the excellent linearity of the OFS response over the entire investigated dose range, with all fitted slopes deviating less than 2% from ideal linearity.

Accuracy evaluations, using alanine dosimetry and radiochromic film as reference methods, demonstrated good agreement across modalities. Relative deviations remained below 1% for most measurements, except for larger discrepancies observed with film dosimetry on the LINAC, which are likely related to film aging effects, batch variability, and inherent energy dependence of the film response.

Energy dependence was assessed using the MultiRad 225 system, revealing small but detectable variations in OFS response as photon energy decreased. The largest deviation of 2.89% was observed at 100 kVp, suggesting a minor energy dependence of the system in the low kV range. Measurements at even lower photon energies remain to be investigated in future work.

The objectives outlined in Section 1.3 have been successfully achieved. Reproducibility, linearity, accuracy, and energy dependence were systematically evaluated for the HS-RP200 across multiple irradiation modalities, while preliminary estimations of the type A uncertainties were performed for all investigated parameters. These analyses provide a first quantification of the statistical variability of the system's measurements.

While the current results demonstrate the excellent dosimetric performance of the HS-RP200, further work remains to complete the full uncertainty budget by incorporating type B uncertainty contributions, including positioning, calibration stability, environmental influences, and long-term system performance. Once fully characterized, the HS-

RP200 system holds strong potential for clinical implementation in routine quality assurance workflows, patient-specific dosimetry verification, and dosimetric audits in both external beam radiotherapy and brachytherapy settings.

References

[1] P. Olko, "Advantages and disadvantages of luminescence dosimetry," *Radiation Measurements*, vol. 45, no. 3-6, pp. 506–511, 2010.

[2] G. Shani, *Radiation Dosimetry. Instrumentation and Methods.* Boca Raton, FL, USA: CRC Press Taylor & Francis Group, 2018.

[3] Medscint Inc., *User Manual for HYPERSCINT Research Platform 200.* Québec, Canada, 2024.

[4] K. Watanabe, "Applications of scintillators in optical-fiber-based detectors," *Japanese Journal of Applied Physics*, vol. 62, 2023. art. no. 010507.

[5] A. Beddar *et al.*, "Water-equivalent plastic scintillation detectors for high-energy beam dosimetry: I. physical characteristics and theoretical considerations," *Physics in Medicine & Biology*, vol. 37, no. 10, pp. 1883–1900, 1992.

[6] A. Beddar *et al.*, "Water-equivalent plastic scintillation detectors for high-energy beam dosimetry: II. properties and measurements," *Physics in Medicine & Biology*, vol. 37, no. 10, pp. 1901–1913, 1992.

[7] M. Koshimizu, "Fundamental processes and recent development of organic scintillators," *Journal of Luminescence*, vol. 278, no. 121008, 2025.

[8] D. Low *et al.*, "Dosimetry tools and techniques for IMRT," *Medical Physics*, vol. 38, no. 3, pp. 1313–1338, 2011.

[9] D. Kobayashi *et al.*, "Impact of CT-based brachytherapy in elderly patients with cervical cancer," *Brachytherapy*, vol. 18, no. 6, pp. 771–779, 2019.

[10] B. Thomadsen and R. Miller, "Electronic brachytherapy devices," in *Comprehensive Biomedical Physics. Volume 9: Radiation Therapy Physics and Treatment Optimization* (A. Brahme, ed.), vol. 9, ch. 9.13, pp. 315–381, New York, USA: Elsevier, 2014.

[11] Precision X-Ray Inc., *MultiRad 160 and 225 User and Technical Manual*, rev. 2.0 ed., Dec. 2018. Accessed: May 2025.

[12] H. Palmans *et al.*, "Dosimetry of small static fields used in external photon beam radiotherapy: Summary of TRS-483, the IAEA-AAPM international code of practice for reference and relative dose determination," *Medical Physics*, vol. 45, no. 11, pp. e1123–e1145, 2018.

[13] Y. Kharzheev, "Radiation hardness of scintillation detectors based on organic plastic scintillators and optical fibers," *Physics of Particles and Nuclei*, vol. 50, no. 1, pp. 42–76, 2019.

[14] S. N. Ahmed, *Physics and Engineering of Radiation Detection*. Amsterdam, Netherlands: Academic Press, Elsevier, 2007.

[15] W. Leo, *Techniques for Nuclear and Particle Physics Experiments: A How-To Approach*. Berlin, Heidelberg, Germany: Springer-Verlag, 2nd ed., 1994.

[16] Medscint Inc., "Scintillation dosimetry," 2024. Available: https://medscint.com/scintillation-dosimetry/. Accessed: Jun. 6, 2025.

[17] Prof. Dr. B. Reniers, "Lecture slides: Relative dosimetry." PowerPoint presentation, 2024. Master of Industrial Engineering: Nuclear Technology, Hasselt University.

[18] A. Micke, A. Lewis, and M. Yu, "Multichannel film dosimetry with nonuniformity correction," *Medical Physics*, vol. 38, no. 5, pp. 2523–2534, 2011.

[19] J. F. P. Albuquerque, E. G. Martins, L. E. E. de Almeida, M. F. de Souza Santos, and J. A. Caldas, "A method for multichannel dosimetry with ebt3 radiochromic films," *Medical Physics*, vol. 41, no. 6, pp. 062101–1 – 062101–10, 2014.

[20] E. Y. L. Ma, H. T. Chiu, J. K. W. Chan, and J. W. C. Chow, "Evaluation of the uncertainty in an ebt3 film dosimetry system utilizing net optical density," *Journal of Applied Clinical Medical Physics*, vol. 17, no. 5, pp. 466–481, 2016.

[21] Prof. Dr. B. Reniers, "Linacs 2 lecture notes." PowerPoint presentation, 2023. Master of Industrial Engineering: Nuclear Technology, Hasselt University.

[22] J. Camps, "Stralingsfysica 2," 2024. Master of Industrial Engineering: Nuclear Technology, Hasselt University.

[23] Prof. Dr. B. Reniers, "Brachytherapy lecture slides," 2024. Master of Industrial Engineering: Nuclear Technology, Hasselt University.

[24] Medscint Inc., "Medscint – company profile," 2024. Available: https://medscint.com/. Accessed: Jun. 4, 2025.

[25] B. Côté, "Scintillation dosimetry: Optimizing radiation therapy with photonics solutions." Medscint Inc., presented at UHasselt, May 2022.

[26] M. Anton, P. Bastian, H. Nowotny, H. Schuhmacher, H. G. Paretzke, W. Ulrich, and P. F. Wojcik, "Response of the alanine/ESR dosimetry system to MV x-rays relative to ^{60}Co radiation," *Physics in Medicine and Biology*, vol. 53, no. 10, pp. 2753–2770, 2008.

[27] Ashland Inc., "Ashland," 2024. Available: https://www.ashland.com/. Accessed: Jun. 6, 2025.

[28] D. Lewis, S. Devic, T. M. Micke, G. B. McCurdy, and A. Chetty, "An efficient protocol for radiochromic film dosimetry combining calibration and measurement in a single scan," *Medical Physics*, vol. 39, no. 10, pp. 6339–6350, 2012.

[29] Seiko Epson Corporation, "Epson corporate information," 2024. Available: https://corporate.epson/en/. Accessed: Jun. 6, 2025.

[30] D. Lewis and S. Devic, "Correcting scan-to-scan response variability for a radiochromic film-based reference dosimetry system," *Medical Physics*, vol. 42, no. 10, pp. 5692–5701, 2015.

[31] D. Lewis and M. F. Chan, "Correcting lateral response artifacts from flatbed scanners for radiochromic film dosimetry," *Medical Physics*, vol. 42, no. 1, pp. 416–429, 2015.

[32] Varian Medical Systems, "Varian medical systems – company profile," 2024. Available: https://www.varian.com/nl/. Accessed: Jun. 6, 2025.

[33] Varian Medical Systems, *TrueBeam Technical Reference Guide*, 2011. Palo Alto, CA, USA.

[34] Varian Medical Systems, "Varian truebeam product brochure: High-precision radiation therapy platform," 2020.

[35] A. Clivio *et al.*, "Volumetric-modulated arc radiotherapy for carcinomas of the anal canal: A treatment planning comparison with fixed field imrt," *Radiotherapy and Oncology*, vol. 92, no. 1, pp. 118–124, 2009.

[36] A. Niroomand-Rad, C. Blackwell, and B. E. C. et al., "Report of aapm task group 235: Radiochromic film dosimetry: Supplement to tg-55," *Medical Physics*, vol. 47, p. 367–418, 2020.

[37] International Atomic Energy Agency (IAEA), "Commissioning and Quality Assurance of Computerized Planning Systems for Radiation Treatment of Cancer," tech. rep., International Atomic Energy Agency, Vienna, Austria, 2004.

[38] Varian Medical Systems, "Varian Medical Systems – LinkedIn Company Profile," 2024. Available: https://www.linkedin.com/company/varian-medical-systems/. Accessed: Jun. 6, 2025.

[39] Varian Medical Systems, *Bravos HDR Afterloader System – Product Overview*, 2020. Available from Varian documentation.

[40] K. M. Cutsinger, K. K. Wong, A. M. Smith, D. J. Crook, J. P. Daly, and W. H. Morrison, "Dosimetric validation and clinical implementation of a novel 24 mm comslike eye plaque using the varian bravos afterloader," *Brachytherapy*, vol. 18, no. 1, pp. 103–110, 2019.

[41] M. J. Rivard, B. M. Coursey, L. A. DeWerd, W. F. Hanson, M. S. Huq, G. S. Ibbott, M. G. Mitch, R. Nath, and J. F. Williamson, "Update of aapm task group no. 43 report: A revised aapm protocol for brachytherapy dose calculations," *Medical Physics*, vol. 31, no. 3, pp. 633–674, 2004.

[42] Xoft, a subsidiary of iCAD, *Axxent Electronic Brachytherapy System Operator Manual*, rev. aj ed., 2017. Accessed: May 2025.

[43] Precision X-Ray Inc., "Precision x-ray – company information," 2024. Available: https://precisionxray.com/. Accessed: Jun. 6, 2025.

[44] Tromp Medical, "Installation Report: Precision X-Ray MultiRad 225, Maastricht UMC," May 2023.

[45] E. Ketels, "A practical guide to designing and validating a brachytherapy QA phantom," Master's thesis, UHasselt and KU Leuven, Diepenbeek, 2025.

[46] OpenAI, "Chatgpt," 2025. [Online]. Available: https://chatgpt.com. Accessed: Jun. 8, 2025.

[47] Joint Committee for Guides in Metrology (JCGM), "Evaluation of Measurement Data – Guide to the Expression of Uncertainty in Measurement (GUM)," Technical Report JCGM 100:2008, Joint Committee for Guides in Metrology, Sèvres, France, 2008.

[48] International Atomic Energy Agency (IAEA), *Absorbed Dose Determination in External Beam Radiotherapy: An International Code of Practice for Dosimetry Based on Standards of Absorbed Dose to Water*. Vienna, Austria: International Atomic Energy Agency, 2024.

[49] C.-M. Ma, J. Seuntjens, K. R. Shortt, D. W. O. Rogers, C. K. Ross, N. V. Klassen, A. Eldib, and M. S. Weinhous, "AAPM protocol for 40–300 kV X-ray beam dosimetry in radiotherapy and radiobiology: Report of Task Group 61 of the AAPM Radiation Therapy Committee," *Medical Physics*, vol. 28, no. 6, pp. 868–893, 2001.

Appendix A

Python script for linearity analysis (LINAC)

The following Python script was used to perform a weighted linear regression on the scintillator data (LINAC) to evaluate its linearity with respect to dose. The absolute uncertainties on each measurement were used as weights. The development of this script was assisted by ChatGPT (OpenAI, 2025) [46], which was used to generate and optimize the code for data analysis purposes.

```
import numpy as np
import matplotlib.pyplot as plt
from scipy.optimize import curve_fit

# Gegevens
dosis = np.array([200, 400, 800, 1600])
signaal = np.array([199.8802, 400.269, 800.02867, 1599.31])
onzekerheden = np.array([0.0197, 0.3267, 0.2842, 0.2102])  # absolute
    onzekerheden

# Lineaire functie
def lineair(x, a, b):
    return a * x + b

# Lineaire fit met gewichten
params, cov = curve_fit(lineair, dosis, signaal, sigma=onzekerheden,
    absolute_sigma=True)
a, b = params
sigma_a, sigma_b = np.sqrt(np.diag(cov))

# R^2 berekenen
signaal_fit = lineair(dosis, a, b)
ss_res = np.sum((signaal - signaal_fit)**2)
ss_tot = np.sum((signaal - np.mean(signaal))**2)
r_squared = 1 - (ss_res / ss_tot)

# Fitlijn genereren voor plot
x_fit = np.linspace(0, 1800, 500)
y_fit = lineair(x_fit, a, b)
```

```
# Errorbars herschalen voor visualisatie
scaling_factor = 100
onzekerheden_scaled = onzekerheden * scaling_factor

# Plot
plt.figure(figsize=(8,6))
plt.errorbar(dosis, signaal, yerr=onzekerheden_scaled, fmt='o',
    capsize=5, elinewidth=1.5,
              markeredgecolor='black', markerfacecolor='blue',
                 ecolor='black', label='Measurements')

plt.plot(x_fit, y_fit, label=f'Fit: y = {a:.3f}x + {b:.3f}\n$R^2$ =
    {r_squared:.5f}',
          color='skyblue', linewidth=2)

plt.xlabel('Set Dose (MU)')
plt.ylabel('Mean OFS Dose (cGy)')
plt.legend()
plt.grid(True, linestyle='--', alpha=0.7)
plt.tight_layout()
plt.show()

# Console output
print("Metingen LINAC:")
print(f"Helling a = {a:.3f} +/- {sigma_a:.3f}")
print(f"Intercept b = {b:.3f} +/- {sigma_b:.3f}")
print(f"R^2 = {r_squared:.5f}")
print(f"NB: error bars scaled by factor {scaling_factor} for visual
    clarity.")
```

Appendix B

Python script for linearity analysis (Bravos)

The following Python script was used to perform a weighted linear regression on the scintillator data (Bravos) to evaluate its linearity with respect to dose. The absolute uncertainties on each measurement were used as weights. The development of this script was assisted by ChatGPT (OpenAI, 2025) [46], which was used to generate and optimize the code for data analysis purposes.

```
import numpy as np
import matplotlib.pyplot as plt
from scipy.optimize import curve_fit

# Gegevens
dosis = np.array([36.6, 109.8, 146.4, 183, 366])
signaal = np.array([36.324, 108.898, 145.758, 182.790, 363.128])
onzekerheden = np.array([0.061, 0.269, 0.360, 0.297, 1.023])  #
    absolute onzekerheden

# Lineaire functie
def lineair(x, a, b):
    return a * x + b

# Lineaire fit met gewichten
params, cov = curve_fit(lineair, dosis, signaal, sigma=onzekerheden,
    absolute_sigma=True)
a, b = params
sigma_a, sigma_b = np.sqrt(np.diag(cov))

# Bereken voorspelde waarden
signaal_fit = lineair(dosis, a, b)

# Bereken R^2
ss_res = np.sum((signaal - signaal_fit)**2)
ss_tot = np.sum((signaal - np.mean(signaal))**2)
r_squared = 1 - (ss_res / ss_tot)

# Fitlijn genereren voor plot
```

```
x_fit = np.linspace(0, 1800, 500)
y_fit = lineair(x_fit, a, b)

scaled_errors = onzekerheden * 5

# Plot
plt.figure(figsize=(8,6))
plt.errorbar(dosis, signaal, yerr=scaled_errors, fmt='o', capsize=8,
    elinewidth=2,
             markeredgecolor='black', markerfacecolor='blue',
                ecolor='black', label='Measurements')

plt.plot(x_fit, y_fit, label=f'Fit: y = {a:.3f}x + {b:.3f}\n$R^2$ =
    {r_squared:.5f}', color='skyblue', linewidth=2)
plt.xlabel('TPS Dose (cGy)')
plt.ylabel('Mean OFS (cGy)')
plt.ylim(0, 400)  # bv. beperkt bereik om kleine errorbars zichtbaar te
    maken
plt.xlim(0, 400)
plt.legend()
plt.grid(True, linestyle='--', alpha=0.7)
plt.tight_layout()
plt.show()

# Console output
print("Metingen Bravos:")
print(f"Helling a = {a:.3f} +/- {sigma_a:.3f}")
print(f"Intercept b = {b:.3f} +/- {sigma_b:.3f}")
print(f"R^2 = {r_squared:.5f}")
```

Appendix C

Python script for PDD analysis (Xoft)

This Python script fits an exponential model to percentage depth dose (PDD) data from the Axxent Xoft measurements. Absolute uncertainties were used as weights in the curve fitting. The script also calculates the R^2 value and visualizes the fit with error bars. The development of this script was assisted by ChatGPT (OpenAI, 2025) [46], which was used to generate and optimize the code for data analysis purposes.

```
import numpy as np
import matplotlib.pyplot as plt
from scipy.optimize import curve_fit

# Gegevens
depth = np.array([2.5, 7.5, 12.5, 17.5])  # mm
mean_dose = np.array([98.6195, 67.0274, 47.6485, 34.3960])  # cGy
uncertainty = np.array([0.1112, 0.0336, 0.0395, 0.0213])  # cGy

# PDD berekenen t.o.v. oppervlakte
pdd = (mean_dose / mean_dose[0]) * 100
pdd_uncertainty = (uncertainty / mean_dose[0]) * 100

# Exponenti le fitfunctie
def exp_fit(x, a, b):
    return a * np.exp(-b * x)

# Curve fit met gewichten
params, cov = curve_fit(exp_fit, depth, pdd, sigma=pdd_uncertainty,
   absolute_sigma=True)
a_fit, b_fit = params
sigma_a, sigma_b = np.sqrt(np.diag(cov))

# Fitwaarden berekenen
pdd_fit = exp_fit(depth, a_fit, b_fit)

# R  berekenen
ss_res = np.sum((pdd - pdd_fit) ** 2)
ss_tot = np.sum((pdd - np.mean(pdd)) ** 2)
r_squared = 1 - (ss_res / ss_tot)
```

```
# Smooth fit curve voor plot
x_fit = np.linspace(0, 20, 300)
y_fit = exp_fit(x_fit, a_fit, b_fit)

# Error bars herschalen
scaling_factor = 10
pdd_uncertainty_scaled = pdd_uncertainty * scaling_factor

# Plot
plt.figure(figsize=(8, 6))
plt.errorbar(depth, pdd, yerr=pdd_uncertainty_scaled, fmt='o',
    capsize=5, elinewidth=1.5,
              markeredgecolor='black', markerfacecolor='blue',
                 ecolor='black', label='Measured PDD')

plt.plot(x_fit, y_fit, label=f'Fit:
    {a_fit:.1f} exp (   {b_fit:.3f} x )\n$R^2$ = {r_squared:.4f}',
          color='skyblue', linewidth=2)

plt.xlabel('Depth (mm)')
plt.ylabel('Mean OFS dose (%)')
plt.grid(True, linestyle='--', alpha=0.7)
plt.legend()
plt.tight_layout()
plt.show()

# Console output
print("Exponenti le fitresultaten:")
print(f"a = {a_fit:.3f} +/- {sigma_a:.3f}")
print(f"b = {b_fit:.5f} +/- {sigma_b:.5f}")
print(f"R^2 = {r_squared:.5f}")
print(f"NB: error bars scaled by factor {scaling_factor} for visual
    clarity.")
```

Appendix D

Python script for linearity analysis (MultiRad 225; 225 kVp)

The following Python script was used to perform a weighted linear regression on the scintillator data (MultiRad 225; 225 kVp) to evaluate its linearity with respect to dose. The absolute uncertainties on each measurement were used as weights. The development of this script was assisted by ChatGPT (OpenAI, 2025) [46], which was used to generate and optimize the code for data analysis purposes.

```
import numpy as np
import matplotlib.pyplot as plt
from scipy.optimize import curve_fit

# Data
set_dose = np.array([100, 200, 400, 600, 800])  # in cGy
ofs_dose = np.array([100.518, 203.244, 405.407, 608.121, 810.119])  #
    in cGy
uncertainty = np.array([0.180, 0.447, 0.497, 0.783, 1.237])  # in cGy

# Linear model
def linear(x, a, b):
    return a * x + b

# Weighted linear regression
params, cov = curve_fit(linear, set_dose, ofs_dose, sigma=uncertainty,
    absolute_sigma=True)
a_fit, b_fit = params
sigma_a, sigma_b = np.sqrt(np.diag(cov))

# Calculate fitted values for R^2
ofs_fit = linear(set_dose, a_fit, b_fit)
ss_res = np.sum((ofs_dose - ofs_fit)**2)
ss_tot = np.sum((ofs_dose - np.mean(ofs_dose))**2)
r_squared = 1 - (ss_res / ss_tot)

# Generate smooth fit line for plotting
x_fit = np.linspace(0, 900, 300)
y_fit = linear(x_fit, a_fit, b_fit)
```

```
# Error bars rescaling
scaling_factor = 20
uncertainty_scaled = uncertainty * scaling_factor

# Plot
plt.figure(figsize=(8, 6))
plt.errorbar(set_dose, ofs_dose, yerr=uncertainty_scaled, fmt='o',
    capsize=5, elinewidth=1.5,
              markeredgecolor='black', markerfacecolor='blue',
                  ecolor='black', label='Measured␣OFS␣dose')

plt.plot(x_fit, y_fit, label=f'Fit:␣y␣=␣{a_fit:.3f}x␣+␣
    {b_fit:.3f}\n$R^2$␣=␣{r_squared:.5f}',
          color='skyblue', linewidth=2)

plt.xlabel('Set␣dose␣(cGy)')
plt.ylabel('Measured␣OFS␣dose␣(cGy)')
plt.grid(True, linestyle='--', alpha=0.7)
plt.legend()
plt.tight_layout()
plt.show()

# Print fit results
print(f"Slope␣(a)␣=␣{a_fit:.5f}␣+/-␣{sigma_a:.5f}")
print(f"Intercept␣(b)␣=␣{b_fit:.5f}␣+/-␣{sigma_b:.5f}")
print(f"R  ␣=␣{r_squared:.5f}")
print(f"Note:␣error␣bars␣scaled␣by␣factor␣{scaling_factor}␣for␣visual␣
    clarity.")
```

Appendix E

Python script for linearity analysis (MultiRad 225; 160 kVp)

The following Python script was used to perform a weighted linear regression on the scintillator data (MultiRad 225; 160 kVp) to evaluate its linearity with respect to dose. The absolute uncertainties on each measurement were used as weights. The development of this script was assisted by ChatGPT (OpenAI, 2025) [46], which was used to generate and optimize the code for data analysis purposes.

```
import numpy as np
import matplotlib.pyplot as plt
from scipy.optimize import curve_fit

# Data
set_dose = np.array([100, 200, 400, 800])  # in cGy
ofs_dose = np.array([102.436, 202.664, 402.656, 803.471])  # in cGy
uncertainty = np.array([0.199, 0.227, 1.289, 4.196])  # in cGy

# Linear model
def linear(x, a, b):
    return a * x + b

# Weighted linear regression
params, cov = curve_fit(linear, set_dose, ofs_dose, sigma=uncertainty,
   absolute_sigma=True)
a_fit, b_fit = params
sigma_a, sigma_b = np.sqrt(np.diag(cov))

# Calculate fitted values for R
ofs_fit = linear(set_dose, a_fit, b_fit)
ss_res = np.sum((ofs_dose - ofs_fit)**2)
ss_tot = np.sum((ofs_dose - np.mean(ofs_dose))**2)
r_squared = 1 - (ss_res / ss_tot)

# Generate smooth fit line for plotting
x_fit = np.linspace(0, 900, 300)
y_fit = linear(x_fit, a_fit, b_fit)

# Error bars rescaling
```

```
scaling_factor = 10
uncertainty_scaled = uncertainty * scaling_factor

# Plot
plt.figure(figsize=(8, 6))
plt.errorbar(set_dose, ofs_dose, yerr=uncertainty_scaled, fmt='o',
    capsize=5, elinewidth=1.5,
              markeredgecolor='black', markerfacecolor='blue',
                 ecolor='black', label='Measured␣OFS␣dose')

plt.plot(x_fit, y_fit, label=f'Fit:␣y␣=␣{a_fit:.3f}x␣+␣
    {b_fit:.3f}\n$R^2$␣=␣{r_squared:.5f}',
          color='skyblue', linewidth=2)

plt.xlabel('Set␣dose␣(cGy)')
plt.ylabel('Measured␣OFS␣dose␣(cGy)')
plt.grid(True, linestyle='--', alpha=0.7)
plt.legend()
plt.tight_layout()
plt.show()

# Print fit results
print(f"Slope␣(a)␣=␣{a_fit:.5f}␣+/-␣{sigma_a:.5f}")
print(f"Intercept␣(b)␣=␣{b_fit:.5f}␣+/-␣{sigma_b:.5f}")
print(f"R  ␣=␣{r_squared:.5f}")
print(f"Note:␣error␣bars␣scaled␣by␣factor␣{scaling_factor}␣for␣visual␣
    clarity.")
```